Supplementary Information

Onset of summer aridification and the decline of *Homo floresiensis* at Liang Bua 61,000 years ago

Michael K. Gagan*, Linda K. Ayliffe, Mika R. Puspaningrum, Gerrit D. van den Bergh, Nick Scroxton, Wahyoe S. Hantoro, Heather Scott-Gagan, Scott A. Condie, R. Lawrence Edwards, Hai Cheng, Jian-xin Zhao, John C. Hellstrom, Alena K. Kimbrough, Matthew J. Gagan, Bambang W. Suwargadi, Joan A. Cowley, Bronwyn C. Dixon, Garry K. Smith, Neil Anderson, Henri Wong, Hamdi Rifai

*Corresponding author: mgagan@uow.edu.au

This file contains:

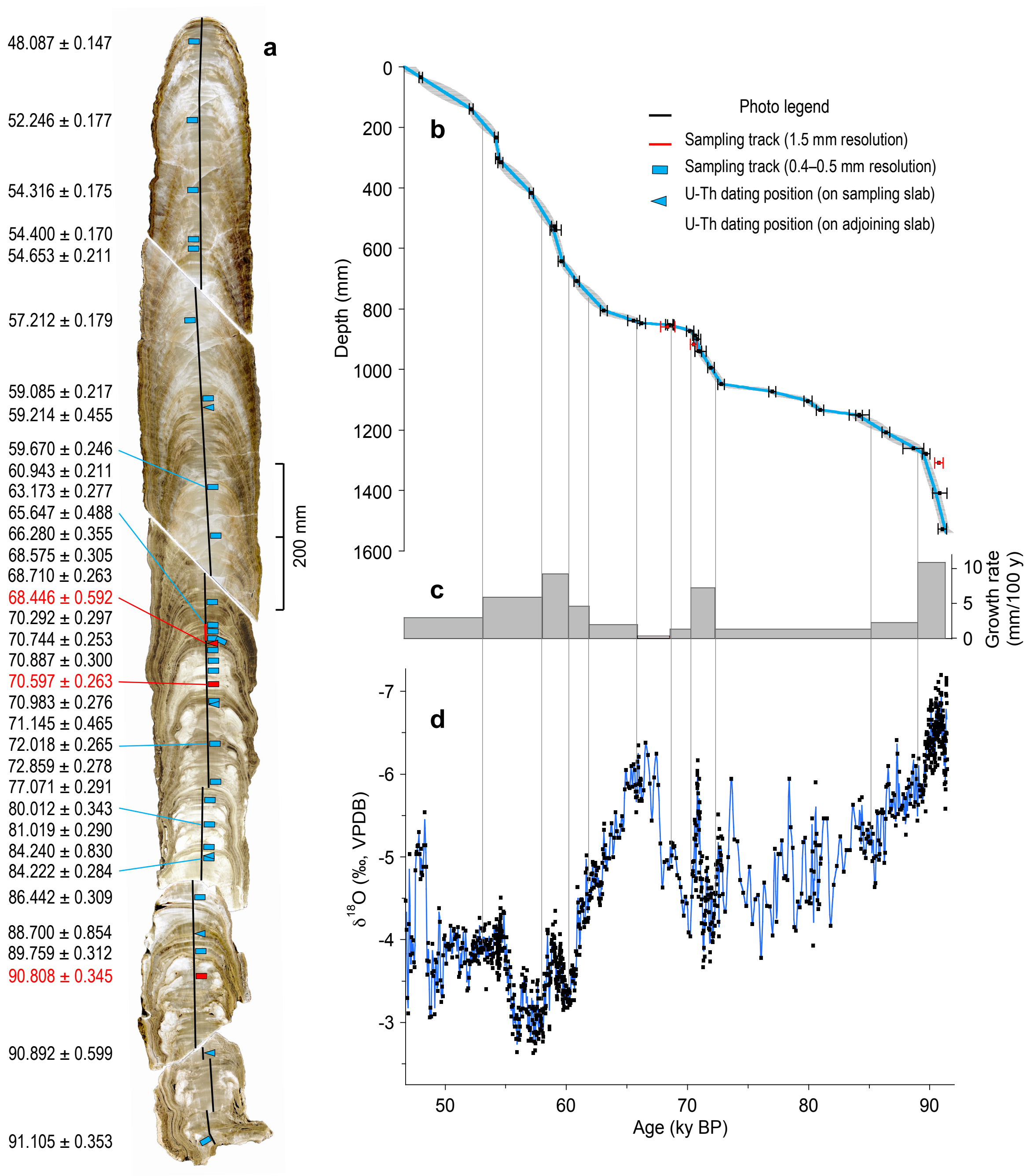

Supplementary Figure 1 | Age model, growth rates and sampling resolution for stalagmite LR09-K2. a Image of polished slab of the stalagmite cut parallel to the central growth axis. The positions of U-Th dates (expressed as ky BP ± 2σ errors) are shown alongside the sampling tracks. **b** Age-depth model (blue line) with 95% confidence interval (grey shading) computed using the OxCal analysis module (version 4.3)[1,2]. Three outlier dates (in red) were excluded to fine tune the age model. **c** Summary of stalagmite growth rates. **d** Distribution of the 1.5-mm sample increments through time. The blue curve shows the fit of the resampled 50-year resolution stalagmite $\delta^{18}O$ record to the raw $\delta^{18}O$ data (black dots). Supplementary Table 1 contains details of the U-Th age data.

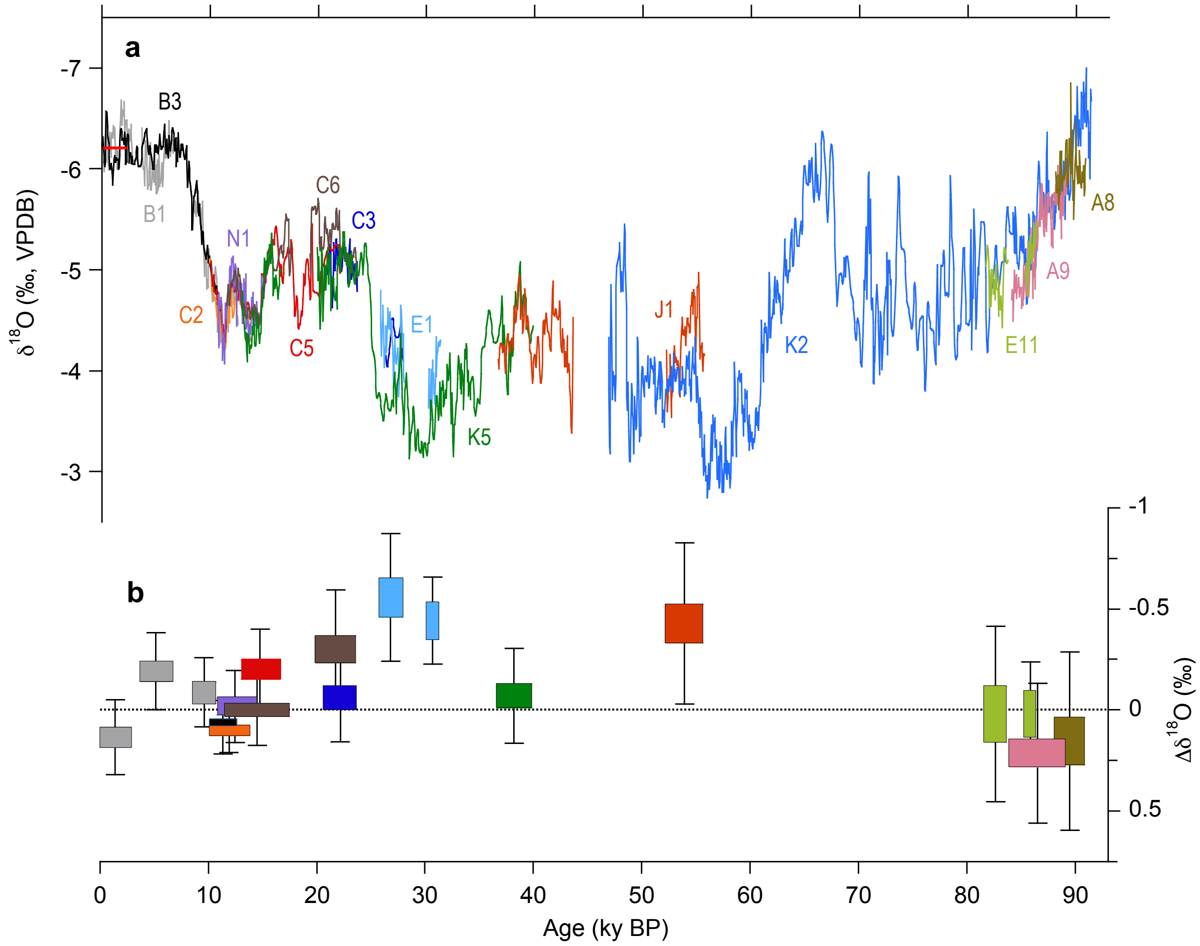

Supplementary Figure 2 | Reproducibility of Liang Luar stalagmite $\delta^{18}O$ records over the past 91,000 years. a Comparison of Liang Luar stalagmite calcite $\delta^{18}O$ records at 50-year resolution (binned data from Scroxton et al.[3]). The new LR09-K2 record is shown in blue. Previously reported records are from Griffiths et al.[4] (LR06-B1, B3), Lewis et al.[5] (LR07-E1), Ayliffe et al.[6] (LR07-C2, C3, C5, C6), Griffiths et al.[7] (LR07-A8, A9, E11) and Scroxton et al.[3] (LR09-N1, J1; LR11-K5). The onset and termination of the LR07-E11 record were not included in the comparison due to the effects of low sample resolution and chronological uncertainties[7]. The section of the LR09-J1 record spanning 52.1–43.6 ky BP was excluded because it is composed of recrystallised, non-primary calcite subject to isotopic overprinting by diagenetic fluids[3]. The red line shows the amount-weighted average stalagmite $\delta^{18}O$ value (–6.2 ± 0.2‰, 2 SE) for summer and winter rainfall conditions at Liang Luar during the Common Era. **b** Summary of differences in stalagmite $\delta^{18}O$ records across overlapping intervals. Colour-coded box plots show the average difference in $\delta^{18}O$ (±2 SE) for 18 intervals ('whiskers' indicate the 2σ range of the differences between data points within each interval). The median absolute difference for 13 overlapping intervals among the 14 stalagmites is 0.09‰ (range, 0.00–0.50‰). The average absolute difference for the three intervals of overlap between the K2 record and the A8, A9 and E11 records (90.875–81.675 ky BP) is 0.13‰. The difference between the K2 and J1 records across 55.675–55.225 ky BP is 0.43‰. These differences are small in the context of the 3.5‰ range in $\delta^{18}O$ for the new K2 record. The good reproducibility of the 14 $\delta^{18}O$ records (derived from widely separated dripwater sites and stalagmites with a broad range of growth rates) shows that they are not compromised by karst controls or in-cave effects in Liang Luar over the last 91,000 years.

Supplementary Note 1. Rayleigh fractionation modelling of the PCP process at Liang Luar

Supplementary Figures 3 and 4 below illustrate the evidence for prior calcite precipitation (PCP) provided by the stalagmite LR09-K2 Mg/Ca, Sr/Ca and Mg/Sr data. The geochemical signature of PCP is governed by Rayleigh fractionation, with Ca^{2+} decreasing exponentially relative to Mg^{2+} and Sr^{2+} in solution[8]. Critically, PCP drives the dripwater concentration of each element away from its initial dissolved bedrock value strictly according to Mg-Ca and Sr-Ca distribution coefficients less than one[9]. We used the Excel-based PCP model developed by Wassenburg et al.[10] to assess the extent of PCP in the LR09-K2 record (Supplementary Fig. 5). The model calculates change in the Mg^{2+} and Sr^{2+}concentrations in dripwater as a consequence of progressive removal of Ca^{2+} by PCP.

The best fit of the model and stalagmite K2 data was achieved using a dolomitic limestone starting composition (52% dolomite) for Liang Luar with an accordingly low Sr concentration (170 ppm), consistent with measurements of Sr in dolomitic limestones[11]. The onset of PCP was assumed to occur at the lowest average Mg/Ca (6.340 mmol/mol) and Sr/Ca (0.0250 mmol/mol) in the K2 record from 91.4 to 82 ky BP. We then tuned the distribution coefficients for Mg/Ca (D_{Mg}) and Sr/Ca (D_{Sr}) to maximise the model fit for the 'target' ln(Sr/Ca) versus ln(Mg/Ca) slope of 0.85 across the full range of the K2 dataset. The best fit for Mg/Ca (range, 6.340–33.535 mmol/mol) requires an initial dolomitic limestone dripwater value of 220 mmol/mol, reaction temperature of 23.5°C, and D_{Mg} of 0.029. The reaction temperature (and hence D_{Mg}) for the calculation was set at an average value of 23.5°C, ~1.5°C below the average pre-industrial air temperature at Liang Luar, as indicated by sea-surface temperature reconstructions for 92–47 ky BP in the Indo-Pacific Warm Pool region[12]. The best fit for Sr/Ca (range, 0.0250–0.1086 mmol/mol) requires an initial dolomitic limestone dripwater value of 0.17 mmol/mol and D_{Sr} of 0.147. The modelled values for D_{Mg} and D_{Sr} fall well within the observed ranges for calcite (0.012–0.06 for D_{Mg}, 0.02–0.3 for D_{Sr}), as summarised by Huang and Fairchild[9] and Sinclair et al.[8].

The model results indicate that PCP is well developed in the K2 record; 82% of Ca^{2+} must be removed from solution to produce the range in Mg/Ca and Sr/Ca observed from 91.4 to 70.3 ky BP and 64.9 to 46.8 ky BP (Supplementary Fig. 5). The modelled best-fit ln(Sr/Ca) versus ln(Mg/Ca) slope (0.88) and observed slope of the K2 data (0.85) are in good agreement, and both ln/ln slopes fall squarely within the theoretical envelope of 0.88 ± 0.13 (ref.[8]).

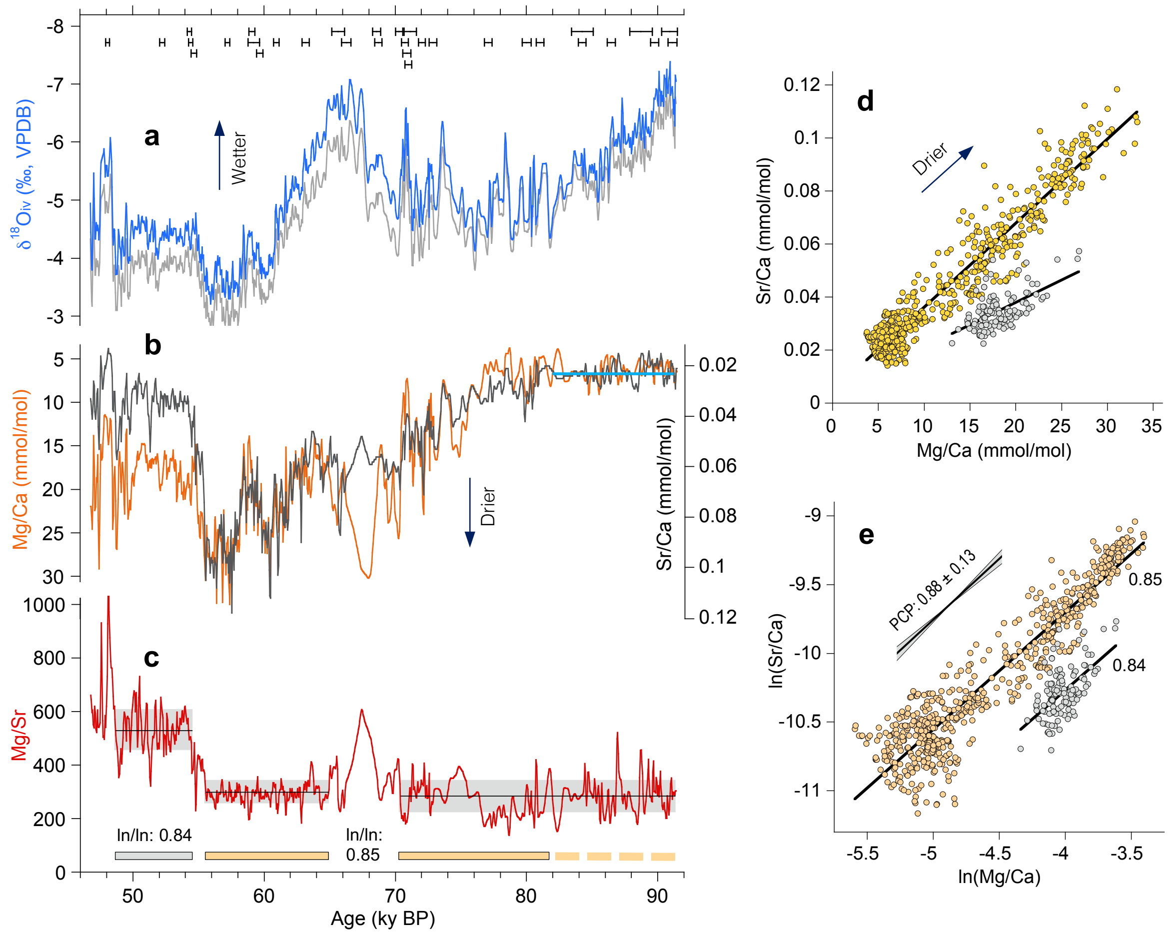

Supplementary Figure 3 | δ^{18}O, Mg/Ca and Sr/Ca and initial PCP analysis for stalagmite LR09-K2. a Adjustment of the 50-year δ^{18}O record (grey) for the influence of ice volume-induced changes in the mean δ^{18}O of seawater ($\delta^{18}O_{iv}$, blue). **b** Positive covariation between the 50-year Mg/Ca (orange) and Sr/Ca (dark grey) records. The best fit across the full range of the data occurs when Mg/Sr is set to 290 (see **c**). Near-constant Mg/Ca and Sr/Ca values between 91.4 and 81.8 ky BP (blue line) mark stalagmite calcite deposition from dripwater with average bedrock Mg/Sr at the initiation of PCP. **c** Stalagmite Mg/Sr. Sections of the record with near-constant Mg/Sr (grey shading is $\pm 1\sigma$) and positive correlation between Mg/Ca and Sr/Ca are indicative of PCP, whereas intervals with anomalous Mg/Sr are influenced by non-PCP processes. The period 70.3–64.9 ky BP, with anomalously high Mg/Sr (and negative correlation between Mg/Ca and Sr/Ca), cannot be interpreted in terms of PCP. Bars at the bottom of the plot show intervals with ln(Sr/Ca) versus ln(Mg/Ca) slopes indicative of PCP. The grey bar shows the PCP-indicative ln/ln slope (0.84) for 54.4–48.6 ky BP, with higher Mg/Sr. **d** Mg/Ca versus Sr/Ca for the intervals with positive correlation and near-constant Mg/Sr (grey is for 54.4–48.6 ky BP). **e** Comparison of ln(Sr/Ca) versus ln(Mg/Ca) with the theoretical PCP slope of Sinclair et al.[8]. The good agreement of the observed slopes (0.84–0.85) with the theoretical slope (0.88 ± 0.13) confirms that most of the LR09-K2 record is controlled by PCP.

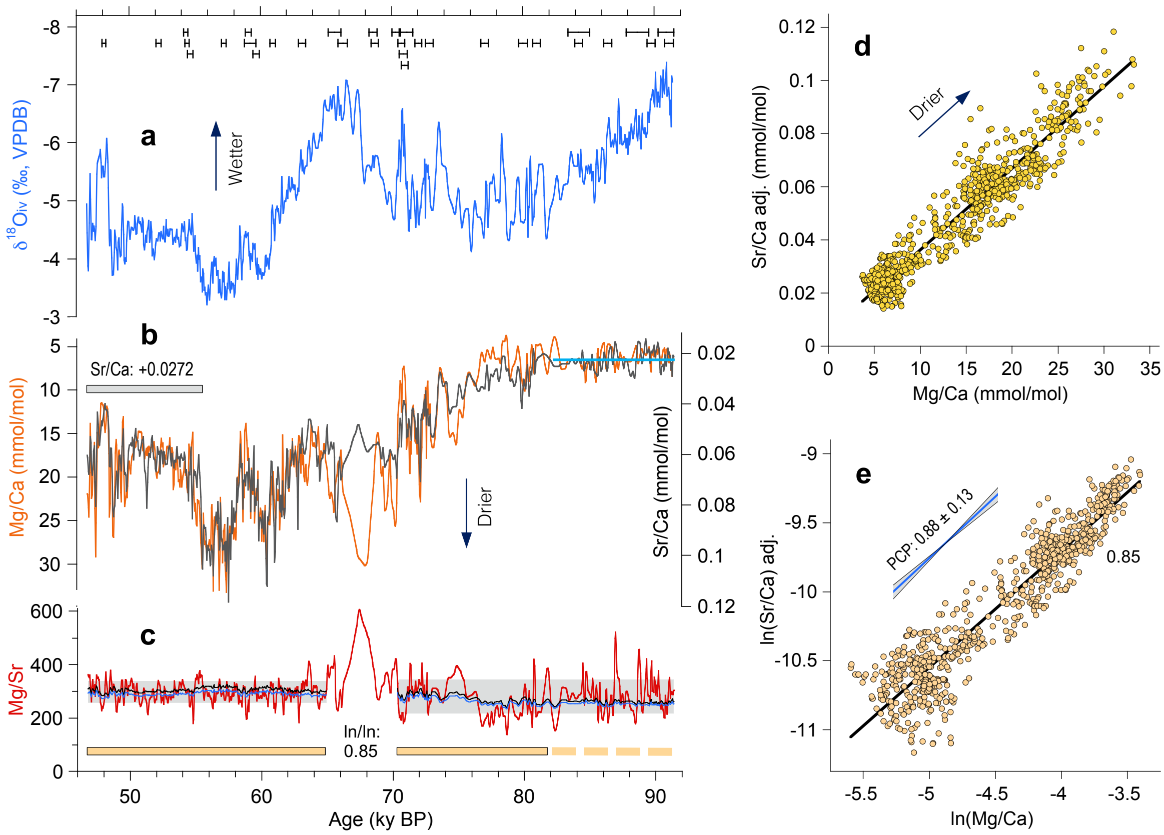

Supplementary Figure 4 | Adjusted δ^{18}O, Mg/Ca and Sr/Ca and refined PCP analysis for stalagmite LR09-K2. **a** The ice-volume corrected δ^{18}O record. **b** Comparison of positive correlation between the Mg/Ca (orange) and Sr/Ca (dark grey) records following adjustment of the Sr/Ca values for 54.4–46.8 ky BP by +0.0272 mmol/mol for alignment with Mg/Ca. The adjoining section (55.5–54.4 ky BP) was adjusted by linear interpolation. **c** Adjusted stalagmite Mg/Sr. The adjustment of Sr/Ca aligns Mg/Sr at a best-fit mean value of 296 ± 37 (1σ, grey shading) from 64.9 to 46.8 ky BP. The ln(Sr/Ca) versus ln(Mg/Ca) slope of 0.85 for the adjusted K2 record (excluding 70.3–64.9 ky BP) is diagnostic of PCP. The black curve shows the least-squares best fit of Mg/Sr for the range of Mg/Ca and Sr/Ca values produced by PCP at ln/ln = 0.85. For comparison, the blue curve shows the good agreement with Mg/Sr produced by PCP at the theoretical ln/ln slope of 0.88 (ref.[8]), as determined by Rayleigh fractionation modelling (see Supplementary Fig. 5e). **d** Adjusted Sr/Ca versus Mg/Ca for the intervals with positive covariation and near-constant Mg/Sr in the K2 record (R^2 = 0.91, excluding 70.3–64.9 ky BP). **e** Comparison of adjusted ln(Sr/Ca) versus ln(Mg/Ca) with the theoretical PCP slope of Sinclair et al.[8]. The good agreement of the observed slope (0.85, R^2 = 0.89) and theoretical slope (0.88 ± 0.13) confirms that the full length of the LR09-K2 record (excluding 70.3–64.9 ky BP) is controlled by PCP.

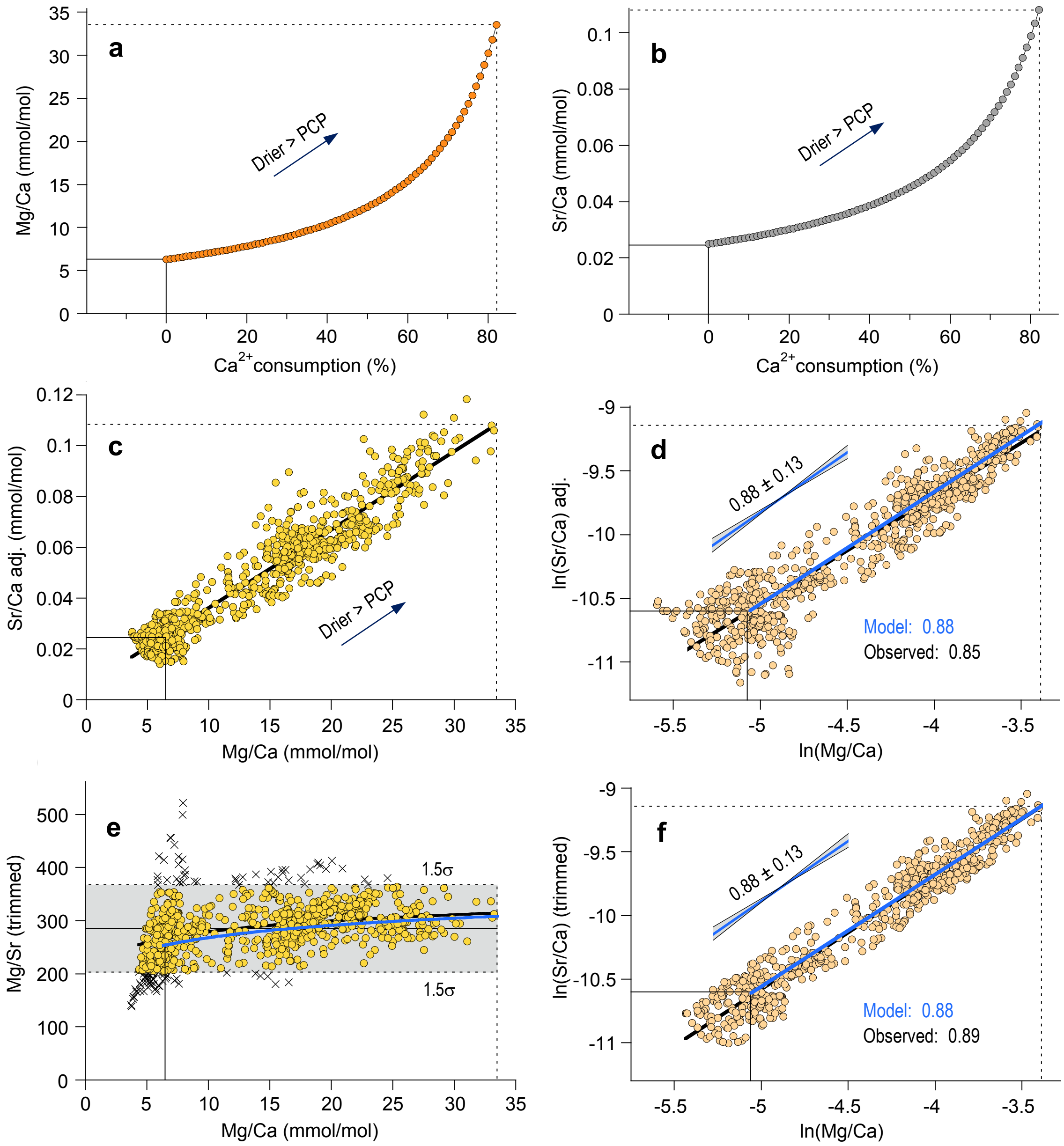

Supplementary Figure 5 | PCP Rayleigh fractionation model for Mg/Ca, Sr/Ca and Mg/Sr in stalagmite LR09-K2. a Stalagmite Mg/Ca as a function of Ca^{2+} consumption from the Excel-based PCP model of Wassenburg et al.[10]. The best fit for Mg/Ca in the K2 record (range, 6.340–33.535 mmol/mol) requires an initial dolomitic limestone dripwater value of 220 mmol/mol, reaction temperature of 23.5°C, and D_{Mg} of 0.029. **b** PCP model for stalagmite Sr/Ca. The best fit for Sr/Ca (range, 0.0250– 0.1086 mmol/mol) requires an initial dolomitic limestone dripwater value of 0.17 mmol/mol and D_{Sr} of 0.147. The model shows that 82% of Ca^{2+} must be removed from solution by PCP to produce the observed range in Mg/Ca and Sr/Ca in the K2 record. **c** Positive correlation between adjusted Sr/Ca and Mg/Ca ($R^2 = 0.91$, excluding 70.3–64.9 ky BP). **d** As for **c**, but for adjusted ln(Sr/Ca) versus ln(Mg/Ca). The agreement of the observed slope (0.85, $R^2 = 0.89$), model slope (0.88) and theoretical PCP slope (0.88 ± 0.13, ref.[8]) confirms that the K2 record is controlled by PCP. **e** Optimisation of the ln/ln model–data fit using stalagmite Mg/Sr. The PCP model (blue curve) shows the subtle logarithmic increase in Mg/Sr as a function of PCP-induced changes in Mg/Ca at ln/ln = 0.88 (mean Mg/Sr, 273; range, 254–310). The K2 stalagmite Mg/Sr also increases with Mg/Ca (black curve), but with more scatter in the data (mean Mg/Sr, 285; range, 139–522). The outlier Mg/Sr values reflect non-PCP processes. 'Trimming' of the K2 Mg/Sr dataset at the 1.5σ level (±80, black crosses) to reduce non-PCP effects optimises the data–model alignment. **f** Comparison of the trimmed and modelled ln(Sr/Ca) versus ln(Mg/Ca). The trimming optimises the data–model fit at ln/ln 0.88–0.89 near the mid-point of the theoretical ln/ln slope envelope (0.88 ± 0.13).

Supplementary Note 2. Modern rainfall and oxygen-isotope climatology at Liang Luar

Establishing the relationship between Mg/Ca and $\delta^{18}O_{iv}$ in stalagmite LR09-K2 and past rainfall requires site-specific information on modern mean annual rainfall, rainfall seasonality and the $\delta^{18}O$ of rainfall at Liang Luar. Previous work has shown that the annual cycles of rainfall and rainfall $\delta^{18}O$ at Liang Luar[4], and elsewhere in southern Indonesia[13], are closely linked. Therefore, it is important to document the modern proportions of summer rainfall (December–March) and 'winter' rainfall (April–November) at Liang Luar contributing to the amount-weighted mean annual $\delta^{18}O$ of cave dripwaters. The approach is valid at Liang Luar where the seasonal contrast in rainfall $\delta^{18}O$ is homogenised in dripwaters, thus allowing stalagmites to consistently record the mean annual $\delta^{18}O$, as demonstrated by good reproducibility of the records (Supplementary Fig. 2).

Rainfall sampling and water-isotope analysis

As no local observational data were available when we began our palaeoclimate investigation in 2006, a rainfall measurement and collection campaign was established for an entire summer monsoon season from September 2006 to April 2007. The rainfall amounts and $\delta^{18}O$ and $\delta^{2}H$ values determined for 39 days with rainfall are summarised in Griffiths et al.[4]. The monitoring site was located adjacent to Rampasasa village, ~700 m from Liang Luar and Luar Bua (see Fig. 1). Rainfall was collected using a standard open-air measuring cylinder and amounts were logged each rain day. Sealed aliquots of the samples were analysed for $\delta^{18}O$ and $\delta^{2}H$ using standard laboratory techniques[4]. All isotopic data are reported as permil (‰) deviations relative to Vienna Standard Mean Ocean Water (VSMOW). The analytical precision (2σ) for replicate measurements of in-run standards was ±0.2‰ for $\delta^{18}O$ and ±2‰ for $\delta^{2}H$.

The 8-month rainwater record for Liang Luar is too short to accurately document the local rainfall climatology so we use monthly rainfall estimates from the NASA Tropical Rainfall Measuring Mission (TRMM) area-averaged satellite product (3B43 V6, 0.25° x 0.25° grid) for context. TRMM data for 1998–2019 are available through the NASA GES DISC Giovanni online data system (https://giovanni.gsfc.nasa.gov/giovanni/) developed by Acker and Leptoukh[14] and Huffman et al.[15]. We also obtained limited rain-gauge data for western Flores from the Global Historical Climatology Network (GHCN) website[16] (version 4; https://ncei.noaa.gov/data/ghcnm/v4beta/access/). Further context is provided by daily rainfall isotope data for the neighbouring island of Bali spanning 2002–2009 compiled by the Institute of Observational Research for Global Change/Japan Agency for Marine-Earth Science and Technology, described by Kurita et al.[13].

Analysis of modern rainfall seasonality

The TRMM rainfall datasets for 1998–2019 provide a reliable measure of rainfall seasonality in western Flores, and were used as a proxy for the rainfall climatology at Liang Luar (Supplementary Fig. 6). However, the area-averaged rainfall seasonality in the TRMM grid-square containing Liang Luar (centred on 8.625° S) is biased by the high proportion of winter rainfall in southern Flores. To prevent bias, we analysed data for adjacent grid squares centred to the north on 8.375° S. These squares provide a reliable measure of the summer-dominated rainfall seasonality immediately 'upstream' of Liang Luar.

Supplementary Figure 6 illustrates the good reproducibility of the percentages of summer rainfall contributing to the mean annual rainfall for the five contiguous grid squares nearest to Liang Luar. The summer rainfall percentage (62.3%) recorded at GHCNv4 World Meteorological Organization (WMO) station 97284002 (Papang, 8.45° S, 12.03° E) is in good agreement with that recorded for the adjacent TRMM grid square (62.6%), supporting the use of the TRMM data as a proxy. Based on this result, the pooled mean rainfall percentage for the five TRMM datasets (61.7 ± 0.6%, 2 SE, for D–M) is used as the contribution of summer rainfall to the amount-weighted mean annual $\delta^{18}O$ of cave dripwaters in the oxygen-isotope mixing model described below in Supplementary Note 3.

Determination of modern mean annual rainfall

The available gridded climate products provide disparate estimates of mean annual rainfall in western Flores, likely due to the complex island topography. Even at fine scale (0.25–0.5°), the effective resolution of the products is determined by the interpolation algorithm and availability of rain-gauge records for calibration. For example, the rain-gauge for the 0.25° TRMM grid square containing Liang Luar is located at Ruteng, which is at higher elevation (1,200 m.a.s.l.) and receives much more rainfall [3,540 mm annually during 53 complete years for 1915–1976 at GHCNv4 WMO station 97284000 (8.65° S, 120.47° E)]. Thus, the TRMM area-averaged mean annual rainfall of 2,099 mm for the grid square is likely too high (Supplementary Fig. 6a).

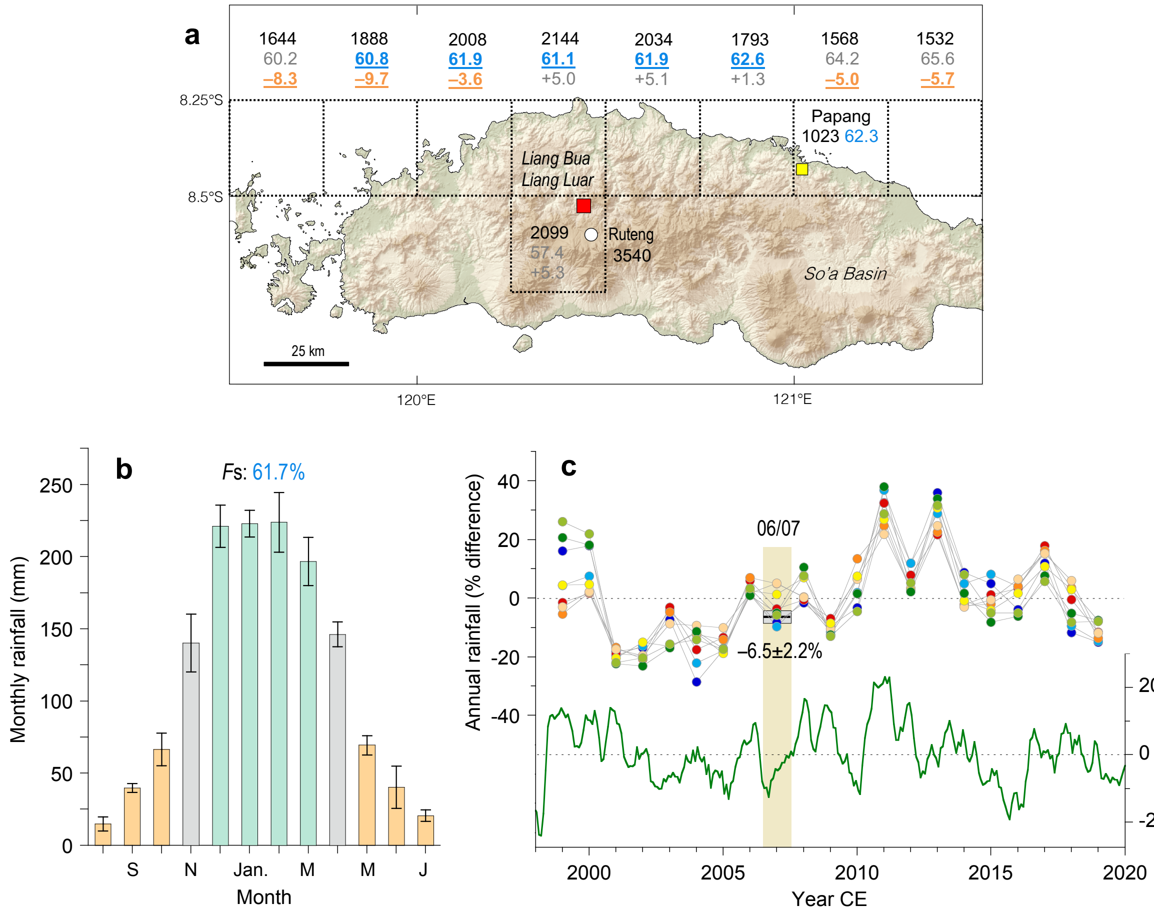

Supplementary Figure 6 | Analysis of rainfall seasonality and mean annual rainfall at Liang Luar. a Locations of rainfall records and summary of rainfall statistics. Black lines indicate 0.25° grid squares for monthly-averaged TRMM satellite records for 1998–2019 (refs.[14,15]). Key rainfall statistics are shown for the eight squares centred on 8.375° S and 119.625–121.375° E used in the analysis: mean annual rainfall (black), summer rainfall percentage (D–M, blue), and percentage difference between annual rainfall in 2006–07 and the long-term mean (orange). For comparison, the yellow square marks the location of rain-gauge data for Papang (WMO station 97284002; 8.45° S, 121.03° E), available from the GHCNv4 website[16] for 1931–1941. The Papang data are in good agreement with TRMM for summer rainfall percentage (blue), but up to ~50% lower than TRMM for mean annual rainfall (black). **b** Modelled rainfall seasonality at Liang Luar. The consistent summer rainfall percentages for the five TRMM records nearest Liang Luar yield an average value of 61.7 ± 0.6% (2 SE) (based on underlined blue values in **a**). The pooled means of the monthly rainfall amounts in these records were used as a proxy for rainfall seasonality at Liang Luar (histogram with black bars showing 2σ range). Grey bars indicate abrupt monsoon transitions in November and April. **c** Determination of mean annual rainfall. In 2006–07, 1,289 mm of rainfall was recorded from September to April at Liang Luar, equating to an annual total of 1,313 mm based on the monthly rainfall distribution in **b**. The result was scaled to mean annual rainfall using the difference between the 2006–07 TRMM data and the longer-term TRMM mean for records centred on 8.375° S. Five records converge on slightly drier conditions in 2006–07 (–6.5 ± 2.2%, 2 SE), consistent with a weak El Niño and negative Southern Oscillation Index (SOI, tan bar). Thus, we adjusted the 2006–07 data by +7%. The resulting mean annual rainfall for Liang Luar is 1,405 ± 33 mm (2 SE). The monthly rainfall values in **b** have been scaled to suit.

As a result, the TRMM rainfall estimate for September 2006–August 2007 is 1,780 mm, whereas only 1,289 mm was recorded for during September 2006–April 2007 at Liang Luar. The 1,289 mm equates to an annual total of 1,313 mm, based on the modelled average monthly distribution of rainfall at Liang Luar (Supplementary Fig. 6b).

Fortunately, the interannual variability across different gridded rainfall products is highly consistent in western Flores. Supplementary Figure 6c shows this strong coherence for 1998–2019 across eight contiguous TRMM records centred on 8.375° S. Therefore, to put the observed rainfall at Liang Luar into context, we scaled the available data for 2006–07 using the difference in mean annual rainfall for 2006–07 (in the TRMM records) and the longer-term TRMM mean.

The year 2006–07 was fairly typical for western Flores in the context of the impact of the El Niño-Southern Oscillation on rainfall. The average difference between the TRMM mean annual rainfall estimates for 2006–07 and the mean for 1998–2019 is –2.6 ± 4.1% (2 SE; range, –9.7 to 5.1%). Five of the records converge on slightly drier conditions in 2006–07 (–6.5 ± 2.2%, 2 SE), consistent with a weak El Niño and negative Southern Oscillation Index. Therefore, to be conservative in our estimates of past aridity, we adjusted the 2006–07 rainfall amount for Liang Luar (1,313 mm) upward by 7% to 1,405 ± 33 mm (2 SE) in accordance with these records. Given the uncertainties in the estimate, we round the results of the analysis to 1,400 mm and allocate 870 mm (62%) to summer (December–March) and 530 mm to 'winter' (April–November) to scale the rainfall history for Liang Luar.

Modern rainfall oxygen-isotope seasonality

We note that the collection of rainfall in an open-air cylinder near Liang Luar entails the risk of day-time evaporation and isotopic enrichment of the samples. However, the $\delta^{18}O$ and $\delta^{2}H$ dataset is orderly and indicates that the daily volumes of collected rainwater were sufficient to mitigate any evaporation effect (Supplementary Fig. 7a). Even dry-season rain-day amounts at Liang Luar between September and November 2006 (n = 15 days) were sizeable, ranging from 3.5 to 40.5 mm d^{-1} (mean, 15.7 mm d^{-1}). The good alignment of $\delta^{18}O$ and $\delta^{2}H$ values for the dry-season samples with the Global Meteoric Water Line indicates that any enrichment of ^{18}O and ^{2}H before collection (or during storage) was negligible (see review by Putnam et al.[17]).

Supplementary Figure 7 shows three key features in the annual cycle of rainfall $\delta^{18}O$ at Liang Luar and in Bali (~700 km west of Flores) that are relevant to the dripwater oxygen-isotope mixing model for the K2 record.

(1) *Dry season uniformity*: The $\delta^{18}O$ of non-convective dry-season rainfall is isotopically uniform at both locations. At Liang Luar, the average $\delta^{18}O$ for non-convective rainfall in September–November 2006 was –1.9‰ VSMOW, similar to the long-term amount-weighted average dry-season value for Bali (–2.6‰ VSMOW for May 2003 to November 2009). The narrow range in $\delta^{18}O$ (–1.7 to –2.6‰) across the large range of the dry-season rainfall in Bali (15–94 mm $month^{-1}$) confirms that a uniform $\delta^{18}O$ value of –2‰ is appropriate for modelling the 40–110 mm $month^{-1}$ range in dry-season rainfall calculated for the K2 record (see Supplementary Note 3).

(2) *Step-changes at monsoon transitions*: Conspicuous shifts to lower (higher) $\delta^{18}O$ occur at the summer monsoon transitions in November (April), signalling the start and end of Intertropical Convergence Zone rainfall associated with deep atmospheric convection. At Liang Luar, the start of the 2006–07 monsoon was accompanied by a ~7‰ decrease in $\delta^{18}O$. These season-specific isotopic domains form the basis for the designation of December–March as summer and April–November as 'winter' in the dripwater mixing model.

(3) *Summer variability*: Although generally low, the $\delta^{18}O$ of daily rainfall in summer at Liang Luar (and at Bali) is highly variable, presumably because of the wide range of daily rainfall amounts and rainfall types in summer. Deep convective rainfall can result in daily mean $\delta^{18}O$ values as low as –15‰ VSMOW, while non-convective rain on very low rainfall days in summer can have positive $\delta^{18}O$ (likely due to enrichment by sub-cloud evaporation[17]). Thus, the dripwater mixing model allows for variation in the $\delta^{18}O$ of convective summer rainfall, in accordance with these 'amount effects'.

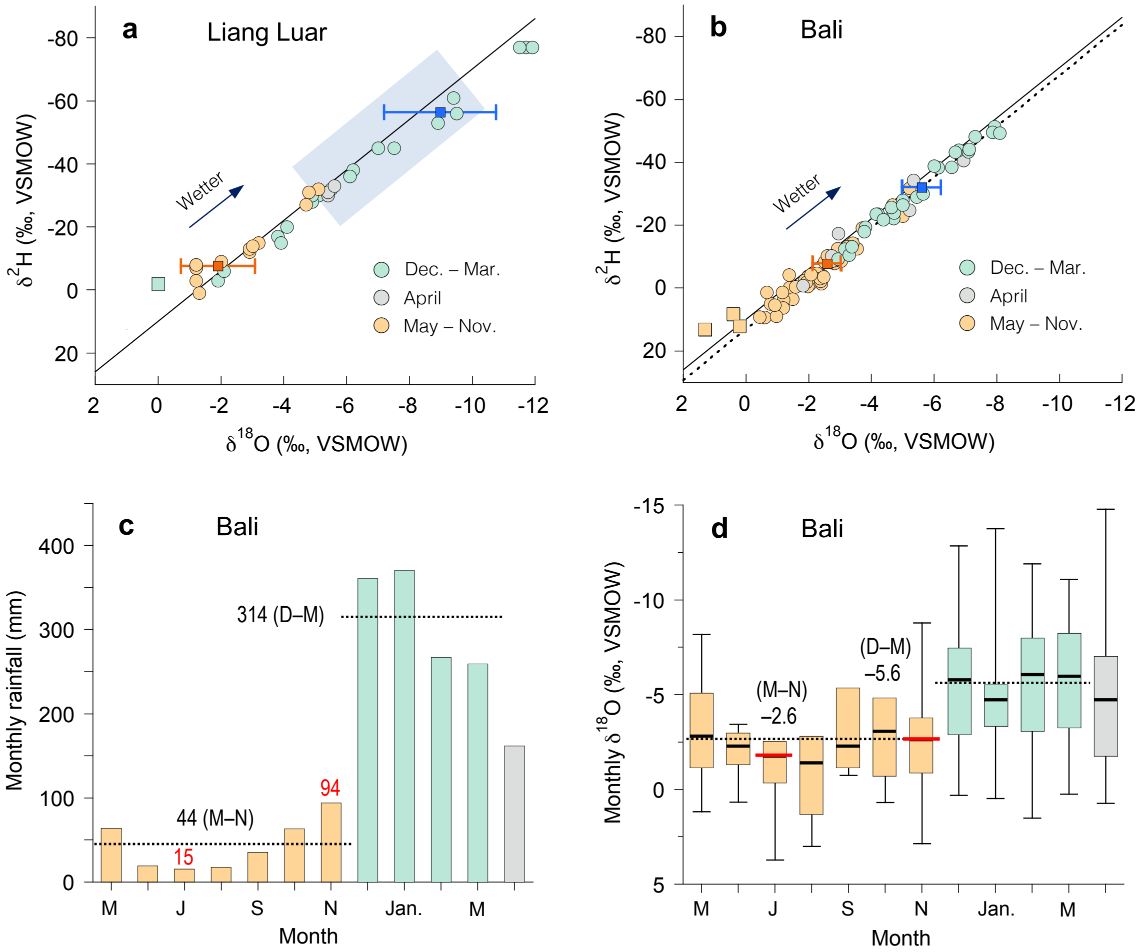

Supplementary Figure 7 | Relationship between rainfall seasonality and δ^{18}O. a Seasonal contrast in δ^{18}O and δ^{2}H at Liang Luar based on 39 rain days between September 2006 and April 2007 (data from Griffiths et al.[4]). The amount-weighted average δ^{18}O values are –9.0 ± 1.8‰ (2 SE) for summer (blue bar) and –1.9 ± 1.2‰ (2 SE) for winter (orange bar). Early April was unusually wet in 2007 and was excluded from the winter analysis (grey circles). Blue shading shows the modelled δ^{18}O range of summer rainfall (–5.0 to –9.6‰) required to produce the range of δ^{18}Oiv in the K2 record (see modelling in Supplementary Note 3). **b–d** Extended analysis of daily rainfall and δ^{18}O measured over seven monsoon cycles in Bali (~700 km west of Flores) for November 2002–November 2009 (based on monitoring data from Kurita et al.[13] near Denpasar; 8.8 °S, 115.12° E; 1 m.a.s.l.). **b** Cross-plot of monthly average δ^{18}O and δ^{2}H of rainfall. Good alignment of the Bali (and Liang Luar) datasets with the Global Meteoric Water Line (black) indicates minimal ^{18}O enrichment of dry-season rainfall (due to sub-cloud evaporation[17]). The dashed local meteoric water line for Bali is shown because the record exceeds the minimum recommended length of 48 months[17]. Only four rain-day samples in **a** and **b** (squares) show slightly elevated δ^{18}O; these were small amounts (0.6–13 mm) and of no significance for the amount-weighted averages. **c** Monthly average rainfall in Bali based on daily observations near the rainfall isotope monitoring site (WMO station 97230; 8.749 °S, 115.167 °E; GHCNv4[16]). April is wetter in Bali than in Flores and was excluded from the δ^{18}O seasonality analysis. **d** Monthly amount-weighted average δ^{18}O of rainfall in Bali (horizontal bars, boxes indicate ranges). Vertical bars indicate range for daily samples. As for Flores, a prominent step-change decrease in δ^{18}O occurs at the summer monsoon transition in November–December. The amount-weighted average dry-season δ^{18}O is –2.6‰, close to the value of –1.9‰ for Flores. Red bars in July and November show the narrow range in δ^{18}O (–1.7 to –2.6‰) across the full range of dry-season rainfall in Bali (15–94 mm month^{-1} in **c**). Monthly average rainfall isotope data for the months of January 2007–November 2009 in Bali were kindly provided by Professor Naoyuki Kurita (Nagoya University) to augment the November 2002–December 2006 dataset published in Kurita et al.[13].

Supplementary Note 3. Dripwater oxygen-isotope mixing model and calculation of rainfall amounts

Supplementary Figures 8–10 below summarise our analysis of the relationships between Mg/Ca and $\delta^{18}O_{iv}$ in stalagmite LR09-K2 and rainfall amounts at Liang Luar. Supplementary Figure 8 illustrates the dripwater oxygen-isotope mixing model that accounts for the effect of summer (December–March) rainfall on stalagmite $\delta^{18}O_{iv}$. The summer in-mixing model applies at times with positive covariation of Mg/Ca and $\delta^{18}O_{iv}$ in the stalagmite K2 record (see Fig. 3). Supplementary Figure 9 accounts for the opposing effects of variable amounts of summer and winter (April–November) rainfall on Mg/Ca and $\delta^{18}O_{iv}$. Supplementary Figure 10 summarises the resulting relationships between Mg/Ca and $\delta^{18}O_{iv}$ and annual, summer and winter rainfall amounts.

Overview and boundary conditions for the mixing model

The relationship between stalagmite $\delta^{18}O_{iv}$ and rainfall was established in the context of an array of binary dripwater $\delta^{18}O$ mixing lines (Supplementary Fig. 8). A generic two end-member oxygen-isotope mass balance equation is sufficient to describe the effect of variable contributions of summer and winter rainfall on stalagmite $\delta^{18}O_{iv}$ at any point within the mixing line array:

$$\delta^{18}O_{iv}\,(\mathrm{VPDB}) = F_w * \delta^{18}O_w\,(\mathrm{VPDB_e}) + F_s * \delta^{18}O_s\,(\mathrm{VPDB_e}) \qquad (1)$$

where $\delta^{18}O_{iv}$ is the amount-weighted annual average $\delta^{18}O$ (VPDB) of stalagmite calcite (corrected for the ice-volume effect); F_w and F_s are the winter and summer rainfall fractions contributing to stalagmite $\delta^{18}O_{iv}$, respectively; and $\delta^{18}O_w$ and $\delta^{18}O_s$ are the amount-weighted average $\delta^{18}O$ values for winter and summer rainfall, respectively, where water-isotope $\delta^{18}O$ values are denoted as $VPDB_e$ (VPDB equivalent, see below).

Periods of positive covariation of Mg/Ca and $\delta^{18}O_{iv}$ in the K2 record can be described by in-mixing of variable amounts of summer rainfall with a fixed amount of winter rainfall. The following boundary conditions were used to describe the effect of summer in-mixing alone on stalagmite $\delta^{18}O_{iv}$:

(1) Winter rainfall was set to 530 mm (the modern average at Liang Luar, Supplementary Fig. 6) with an average $\delta^{18}O$ of –2‰ $VPDB_e$, consistent with the uniform modern-day average isotopic value of non-convective winter rainfall at Liang Luar[4] and at low-elevation sites in the region[13] (Supplementary Fig. 7).

(2) The $\delta^{18}O$ of summer rainfall was allowed to vary inversely with summer rainfall amount, in accordance with rainfall $\delta^{18}O$ data for Liang Luar[4] and elsewhere in southern Indonesia[13]. Thus, each binary mixing line in the array is associated with a specific summer rainfall amount linked to a compatible value of $\delta^{18}O_s$.

The relationship between stalagmite $\delta^{18}O_{iv}$ and summer rainfall in the array was scaled using two conditions:

(1) The wetter interglacial end of the mixing model was scaled using the modern-day relationship between stalagmite $\delta^{18}O_{iv}$ and rainfall at Liang Luar. In Supplementary Figure 8, the binary mixing line defining modern-like climate conditions is set to intersect the modern average $\delta^{18}O_{iv}$ (–6.2‰) when the summer rainfall fraction in dripwater (F_s) is 0.6214 (defined by 870/1,400 mm; see Supplementary Figs. 2, 6).

(2) The start point for summer in-mixing was set under the condition of no convective summer monsoon rainfall, such that the $\delta^{18}O$ values of summer and winter rainfall are equal (–2‰) when the average summer rainfall rate (over 4 months) is equal to the average winter rainfall rate (over 8 months). At this point, F_s = 0.333 (defined by 265/795 mm) and stalagmite $\delta^{18}O_{iv}$ = –2‰.

We note that Liang Luar stalagmite calcite $\delta^{18}O$ values (on the VPDB scale) are essentially equivalent to rainfall $\delta^{18}O$ values (on the VSMOW scale), and thus comparable for the purposes of the model. Hence, water-isotope $\delta^{18}O$ values (VSMOW) are denoted as $VPDB_e$ (VPDB equivalent). Previous work has shown that the numerical difference in $\delta^{18}O$ between modern dripwaters and stalagmite calcite at Liang Luar is only 0.6‰. The average $\delta^{18}O$ for dripwaters and pool waters collected at Liang Luar during the 2007 dry season (n = 7) is –5.49 ± 0.04‰ VSMOW (± SE)[18]. Similarly, the average $\delta^{18}O$ for modern stalagmite calcite in Liang Luar is –6.06 ± 0.05‰ VPDB (± SE, n = 2 measurements performed at the ANU Research School of Earth Sciences)[6].

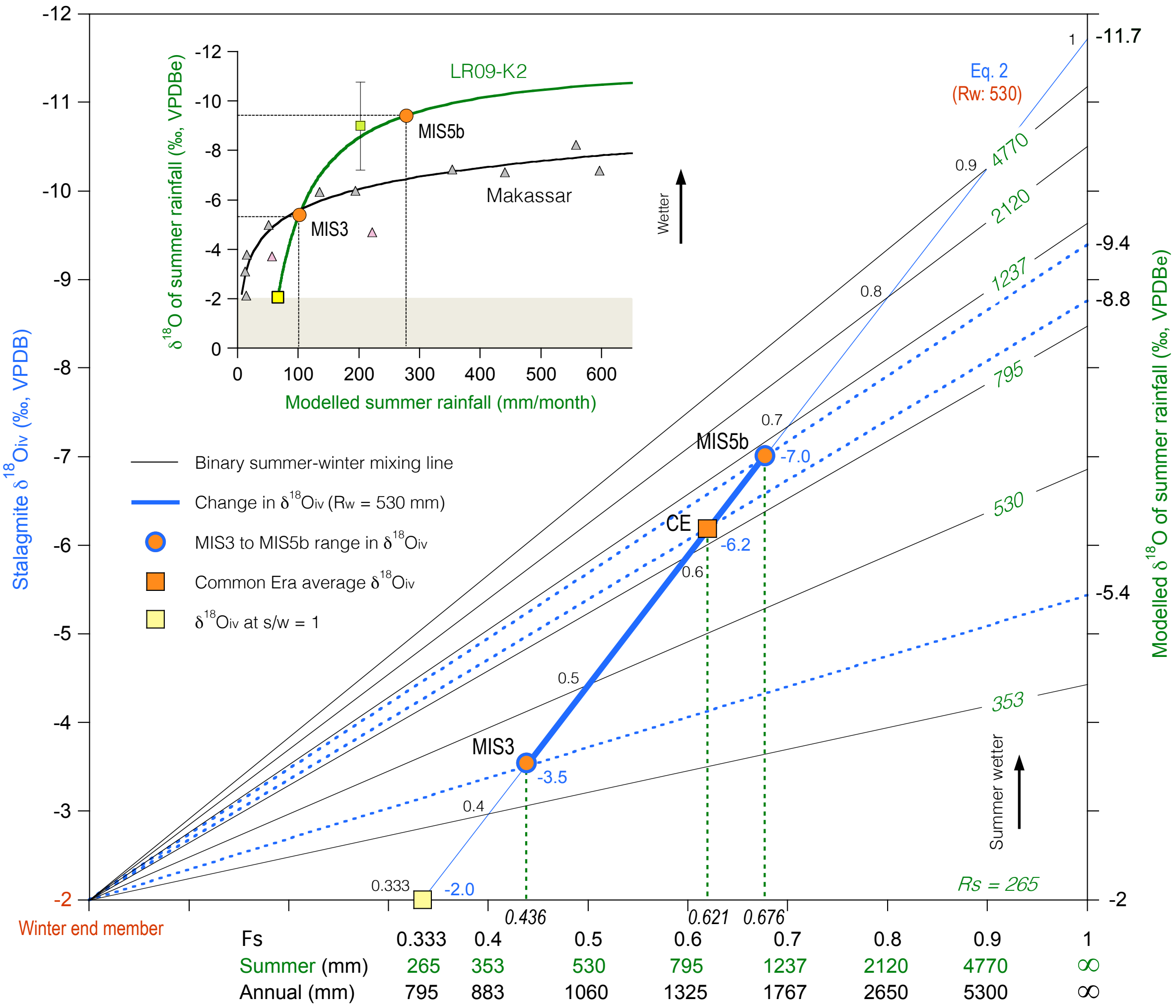

Supplementary Figure 8 | Summer rainfall in-mixing model for stalagmite LR09-K2. The relationship between stalagmite δ^{18}Oiv and summer rainfall for times of positive covariation in Mg/Ca and δ^{18}Oiv is shown in the context of an array of binary dripwater δ^{18}O mixing lines (example lines are in grey). The slopes of the lines are set by in-mixing of summer rainfall (R_s) with variable δ^{18}O (y axis on right) with winter rainfall (R_w) at 530 mm and δ^{18}O = –2‰. The relationship between δ^{18}Oiv and summer in-mixing (δ^{18}Osi, bold blue line) is scaled to the modern average stalagmite δ^{18}Oiv (–6.2‰) at F_s = 0.6214 (870/1,400 mm, orange square). The yellow square at δ^{18}Osi = –2‰ marks the start point for measurable summer in-mixing at F_s = 0.333 (265/795 mm), when the summer and winter rainfall rates are equal (s/w = 1). The resulting relationship is: δ^{18}Osi = –14.58F_s + 2.86 (see Eq. 2). Corresponding summer (green) and annual (black) rainfall amounts are scaled to F_s on the x axis. Importantly, each binary mixing line is associated with a specific summer rainfall amount (green) linked to a compatible summer rainfall δ^{18}O value (y axis on right). Supplementary Figure 9 illustrates how a change in winter rainfall moves the measured δ^{18}Oiv value along a specific binary mixing line (away from the summer in-mixing line defined for winter at 530 mm). The inset plot shows the logarithmic relationship between the modelled δ^{18}O of summer rainfall and modelled summer rainfall amount (green curve). The model curve (at –8.8‰) is in close agreement with the modern amount-weighted mean summer rainfall δ^{18}O value recorded at Liang Luar[4] (–9.0 ± 1.8‰, 2 SE, pale green square with bars). For comparison, the black curve shows the modern-day relationship between mean monthly rainfall and rainfall δ^{18}O at Makassar, south-western Sulawesi, for November 2002–December 2006 (ref.[13]). Pink triangles mark high δ^{18}O outliers in October and November (end of the dry season) that were not included in the regression. The results illustrate the sensitivity of rainfall δ^{18}O to rainfall amount in drier climates, and its limitations under conditions of high rainfall produced by well-organised deep atmospheric convection. The relatively dry hydroclimate at Liang Luar between MIS 5b and MIS 3 falls well within the model's viable range (see Supplementary Note 3 Box 1 below for details).

Adjustment of the $\delta^{18}O_{iv}$ (VPDB) values by +0.6‰ to match SMOW would slightly increase the sensitivity of the modelled rainfall amounts to changes in $\delta^{18}O_{iv}$. Thus, for conservative reconstruction, $\delta^{18}O_{iv}$ values remain on the VPDB scale. Also, we do not correct for the non-identical scaling of delta values on the VPDB and VSMOW scales[19], given that the net distortion is exceedingly small over the 3.5‰ range in $\delta^{18}O_{iv}$ in the K2 record (always <0.11‰). Supplementary Figure 8 shows that the approach is valid, as the modelled $\delta^{18}O$ for modern summer rainfall (–8.8‰ VPDBe) is in good agreement with the modern amount-weighted mean $\delta^{18}O_s$ at Liang Luar (–9.0 ± 1.8‰ VSMOW, 2 SE)[4] with $\delta^{18}O_{iv}$ and F_s set at –6.2‰ and 0.6214.

Based on Supplementary Figure 8, the relationship between the stalagmite K2 $\delta^{18}O_{iv}$ and in-mixing of summer rainfall with 530 mm of winter rainfall ($\delta^{18}O_{si}$) can be expressed as:

$$\delta^{18}O_{si} = -14.58Fs + 2.86 \tag{2}$$

Recall that the lower limit on F_s is 0.333 under conditions of no convective summer monsoon rainfall (when the summer and winter rainfall rates are equal), and at this point stalagmite $\delta^{18}O_{iv}$ equates to –2‰. Thus Eq. 2 shows, in principle, that the theoretical range for Liang Luar stalagmite $\delta^{18}O_{iv}$ (50-year average) due to summer rainfall alone extends from –2‰ to –11.7‰ (VPDB) for F_s = 0.333 to 1. However, the relatively small range in $\delta^{18}O_{iv}$ in the K2 record (–3.5‰ to –7‰) can be produced by a modest range in summer monsoon rainfall (44–68% of the mean annual rainfall). The stability of the relationship between $\delta^{18}O_{iv}$ and rainfall amount through time is evident in lengthy stalagmite Mg-^{18}O records from south-western Sulawesi, near Flores. In Sulawesi, stalagmite Mg/Ca and $\delta^{18}O_{iv}$ are both dictated largely by summer rainfall and the available records define a consistent shift in $\delta^{18}O_{iv}$ across each glacial-interglacial climate transition (2.7–3.0‰, n = 3)[20,21].

Determination of rainfall amounts

Supplementary Figure 9 below illustrates the full solution of the mixing model used to calculate mean annual rainfall (R_a), summer rainfall (R_s) and winter rainfall (R_w) amounts from the K2 Mg-^{18}O record. This model accounts for changes in R_w, with relatively high $\delta^{18}O$, that drive negative covariation of stalagmite Mg/Ca and $\delta^{18}O_{iv}$ (see Fig. 3), and the resulting offsets in $\delta^{18}O_{iv}$ from the summer in-mixing line defined by Eq. 2 (where R_w is constant at 530 mm).

The relationship between $\delta^{18}O_{iv}$ and the unique mixture of summer and winter rainfall compatible with each Mg-^{18}O data pair in the K2 record is defined by one binary mixing line within the model array. The generic equation for each binary line that must be identified is:

$$\delta^{18}O_{iv} = m\left(\frac{R_s}{R_a}\right) - 2 \tag{3}$$

Here, F_s is expressed in terms of rainfall (R_s/R_a). The y-intercept for every line is –2‰ (VPDBe), the regional average $\delta^{18}O$ value for non-convective winter rainfall (as defined in Supplementary Fig. 8). Thus, the key step is to identify the values of m (line slope), R_s and R_a that bring the calculated value for $\delta^{18}O_{iv}$ into precise alignment with the measured $\delta^{18}O_{iv}$. The identification of a compatible binary mixing line is required for each of the 893 Mg-^{18}O data pairs in the K2 record.

Importantly, R_a can be directly determined from the measured values of Mg/Ca (see Eq. 8 below). And R_s and m are both defined by an associated value of $\delta^{18}O_{si}$ at the point where each mixing line intersects the summer rainfall in-mixing line (defined by Eq. 2). Therefore, finding the value of $\delta^{18}O_{si}$ that satisfies each Mg-^{18}O data pair is critical for determining R_s. Once R_s is known, R_w is the difference between R_s and R_a.

The steps required to identify $\delta^{18}O_{si}$ and the combination of m, R_s and R_a that brings Eq. 3 into agreement with the measured $\delta^{18}O_{iv}$ are described below. First, we define m, R_s and R_a in terms of $\delta^{18}O_{si}$. The relationship between $\delta^{18}O_{si}$ and F_s in Eq. 2 can be re-expressed to define m in terms of $\delta^{18}O_{si}$:

$$m = \frac{-14.58(\delta^{18}O_{si} + 2)}{\delta^{18}O_{si} - 2.86} \tag{4}$$

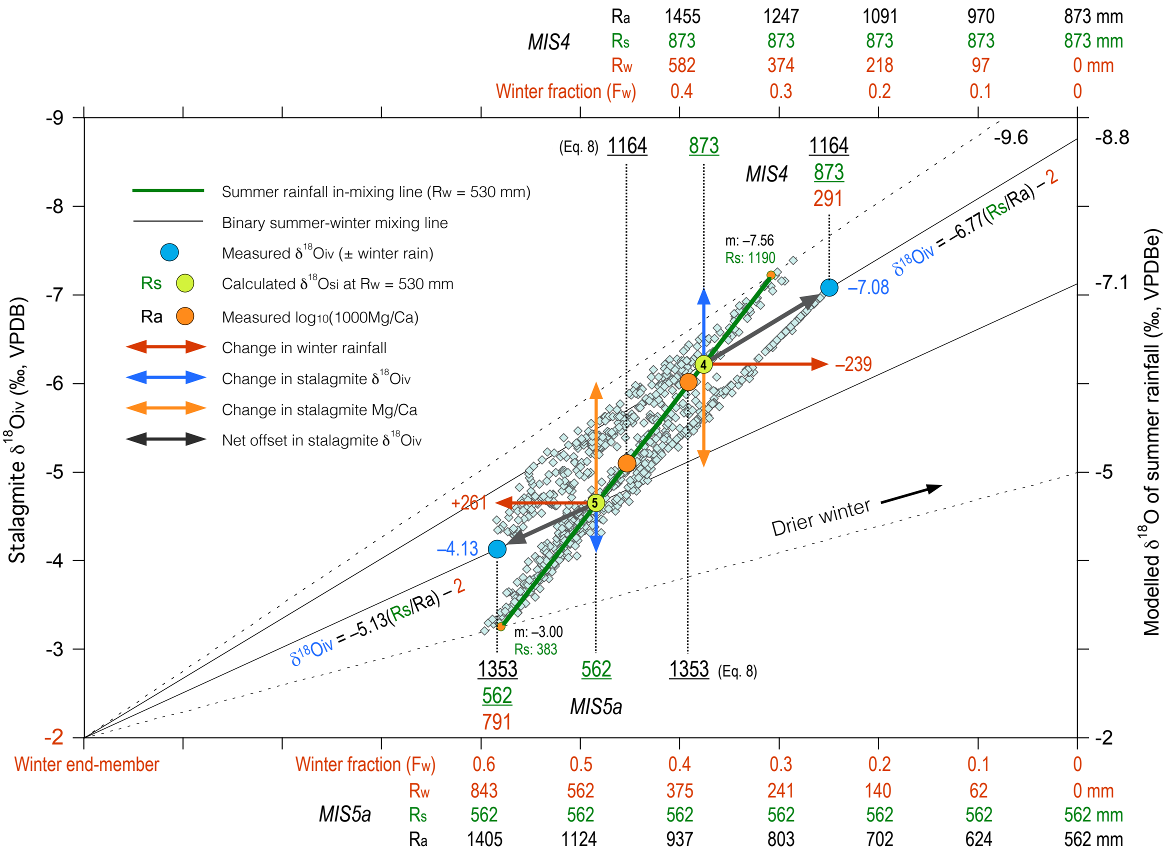

Supplementary Figure 9 | Generalised mixing model for stalagmite LR09-K2. The generalised mixing model accounts for changes in winter rainfall (*R*w) that drive negative covariation of stalagmite Mg/Ca and $\delta^{18}O_{iv}$. Changes in *R*w offset the measured $\delta^{18}O_{iv}$ values (blue diamonds) from the summer in-mixing line (Eq. 2 green line with *R*w constant at 530 mm). The exact position of each $\delta^{18}O_{iv}$ data point in the mixing line array (*n* = 893 points) is controlled by the change in *R*w along one binary mixing line (4 examples in grey), each associated with a specific summer rainfall amount (*R*s) and compatible summer rainfall $\delta^{18}O$ value (*y* axis on right). The resulting $\Delta^{18}O_{iv}/\Delta F_s$ slopes of the lines (*m*) change from –3.00 to –7.56 in accordance with the range in *R*s. To account for the effects of winter rainfall on $\delta^{18}O_{iv}$, we identified the specific mixing line slope (Eq. 4), and co-dependent values of $\delta^{18}O_{si}$ and *R*s on the summer in-mixing line (Eq. 10), that reconciled the offset in $\delta^{18}O_{iv}$ from the summer line. To illustrate the method, vector analyses are shown for two contrasting winter rainfall scenarios: a 239-mm decrease in *R*w during MIS 4 (the 66.525 ky BP Mg-^{18}O data pair) and a 261-mm increase during MIS 5a (the 76.075 ky BP Mg-^{18}O data pair). The grey vectors show how the opposing changes in *R*w drive stalagmite $\delta^{18}O_{iv}$ in opposite directions from the $\delta^{18}O_{si}$ 'start points' (pale green circles). The upper and lower *x* axes highlight the different scales of the changes in *R*w (orange) and *R*a (black) due to the different mixing line slopes for MIS 4 (–6.77, upper *x* axis) and MIS 5a (–5.13, lower *x* axis). Orange circles show the associated (opposing) shifts in mean annual rainfall (*R*a, based on the measured Mg/Ca and Eq. 8) away from the $\delta^{18}O_{si}$ 'start points' along the summer line (scaled to $\delta^{18}O$). Colour-coded text indicates the calculated values of *R*a, *R*s and *R*w that are uniquely compatible with the Mg-^{18}O data pairs defining both scenarios.

Each binary mixing line is associated with a specific summer rainfall amount. Thus, the value of *R*s for each binary line is defined by $\delta^{18}O_{si}$ at its point of intersection with the summer rainfall in-mixing line (defined by Eq. 2). The relationship between $\delta^{18}O_{si}$ and *R*s is given by Eq. 2 with *F*s expressed in terms of *R*s and *R*w:

$$\delta^{18}O_{si} = -14.58\left(\frac{Rs}{Rs + Rw}\right) + 2.86 \tag{5}$$

Equation 5 serves to scale *R*s to $\delta^{18}O_{si}$ along the summer rainfall in-mixing line in Supplementary Figures 8 and 9. Substitution of 530 mm for *R*w and rearrangement of Eq. 5 yields *R*s as a function of $\delta^{18}O_{si}$:

$$R_s = \frac{1515.8 - 530\delta^{18}O_{si}}{\delta^{18}O_{si} + 11.72} \tag{6}$$

Addition of 530 mm (R_w) to Eq. 6 and simplification yields R_a:

$$R_a(^{18}O) = \frac{7727.4}{\delta^{18}O_{si} + 11.72} \tag{7}$$

Importantly, Eq. 7 provides a means to calibrate the relationship between stalagmite Mg/Ca and R_a, which is independent of changes in seasonality. The log-linear relationship $\delta^{18}O_{iv} = 4.822*\log_{10}(1000Mg/Ca) - 10.56$ (defined in the main text Fig. 3) is used for the transformation. Substitution of this relationship for $\delta^{18}O_{si}$ in Eq. 7 yields a general equation for calculating R_a for every Mg-^{18}O data pair in the K2 record:

$$R_a = \frac{1602.5}{\log_{10}(1000Mg/Ca) + 0.2406} \tag{8}$$

With m and R_s defined in terms of $\delta^{18}O_{si}$, the expanded version of Eq. 3 is:

$$\delta^{18}O_{iv} = \frac{-14.58(\delta^{18}O_{si} + 2)}{\delta^{18}O_{si} - 2.86} * \left[\frac{\left(\frac{1515.8 - 530\delta^{18}O_{si}}{\delta^{18}O_{si} + 11.72}\right)}{R_a}\right] - 2 \tag{9}$$

In this form, Eq. 9 defines the specific value of $\delta^{18}O_{si}$ (and hence m and R_s) required to solve Eq. 3 and bring the calculated value for $\delta^{18}O_{iv}$ into precise alignment with the measured $\delta^{18}O_{iv}$. Therefore, to find the mixing line specific to each Mg-^{18}O data pair, we solve Eq. 9 for $\delta^{18}O_{si}$ as a function of the measured $\delta^{18}O_{iv}$ and associated R_a (from Eq. 8):

$$\delta^{18}O_{si} = \frac{R_a(-11.72\delta^{18}O_{iv} - 23.44) + 15454.8}{R_a\delta^{18}O_{iv} + 2R_a - 7727.4} \tag{10}$$

R_s can then be calculated from the resulting $\delta^{18}O_{si}$ (using Eq. 6).

The final step is to determine R_w as the difference between R_a and R_s:

$$R_w = R_a - R_s \tag{11}$$

Supplementary Data 2 summarises the five key steps (Eqs. 4, 6, 8, 10, 11) required to identify the mixing line slope and values of R_a, R_s and R_w compatible with each Mg-^{18}O data pair in the K2 record.

To illustrate the generalised model, Supplementary Figure 9 shows a vector analysis of two contrasting winter rainfall scenarios: a 239-mm decrease in R_w during MIS 4 (at 66.525 ky BP) and a 261-mm increase during MIS 5a (at 76.075 ky BP). These opposing changes in R_w drive stalagmite $\delta^{18}O_{iv}$ in opposite directions away from the summer rainfall in-mixing line. Note that the impact of R_w on Mg/Ca and $\delta^{18}O_{iv}$ varies as a function of mixing line slope.

Summary of rainfall results

Supplementary Figure 10 below illustrates the relationships between R_a, R_s and R_w and the K2 Mg-^{18}O system. The modelled range in R_a for $\log_{10}(1000Mg/Ca)$ values spanning 0.570–1.522 mmol/mol in the K2 record (based on Eq. 8) is 909 mm at 57.375 ky BP (MIS 3) to 1,977 mm at 78.625 ky BP (MIS 5a). The relationship of R_s and $\delta^{18}O_{iv}$ is shown for times of positive covariation of Mg/Ca and $\delta^{18}O_{iv}$ (based on Eq. 6). The modelled range extends from 378 mm at 55.925 ky BP (MIS 3) to 1,255 mm at 90.925 ky BP (MIS 5b).

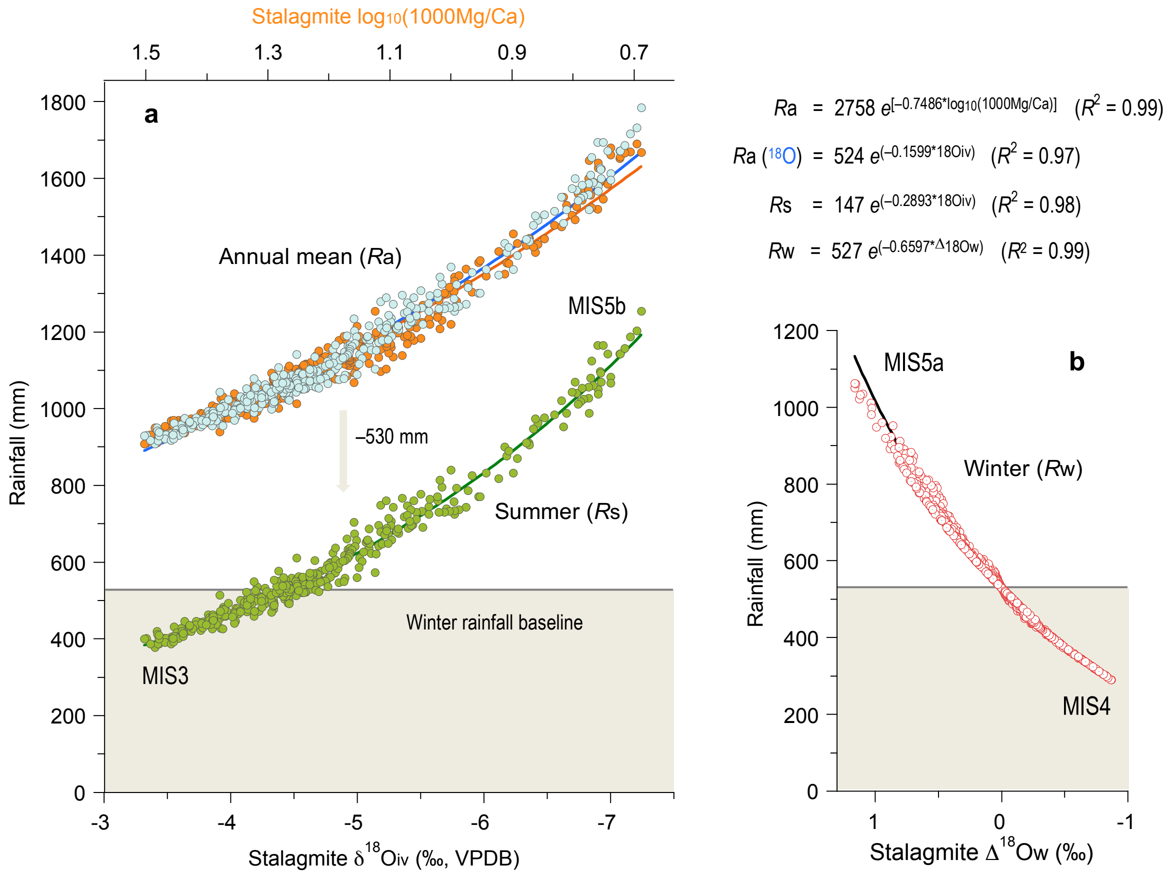

Supplementary Figure 10 | Relationships between stalagmite Mg-^{18}O and annual, summer and winter rainfall at Liang Luar. a Exponential relationships between the stalagmite K2 Mg-^{18}O system and mean annual rainfall (R_a) and summer rainfall (R_s), based on the summer rainfall in-mixing model (Supplementary Fig. 8). Mg/Ca was scaled to $\delta^{18}O_{iv}$ using the log-linear relationship for the three calibration intervals in the K2 record with positive covariation of Mg/Ca and $\delta^{18}O_{iv}$: 91.375–89.575, 75.475–70.325 and 60.275–46.775 ky BP (see main text Fig. 3). The average absolute difference between $R_a(^{18}O)$ (based on Eq. 7) and R_a (based on Eq. 8) is 38 ± 69 mm (2σ, n = 412 Mg-^{18}O data pairs). The relationship of $\log_{10}$(1000Mg/Ca) and R_a is independent of changes in seasonality and thus represents a general calibration for R_a for every Mg-^{18}O data pair in the K2 record. The lower curve (green) shows the relationship between R_s and stalagmite $\delta^{18}O_{iv}$ (based on Eq. 6) after subtraction of the baseline contribution of winter rainfall (530 mm). **b** Relationship between R_w and the difference between the measured $\delta^{18}O_{iv}$ and associated $\delta^{18}O_{si}$ on the summer in-mixing line ($\Delta^{18}O_w$), based on Eq. 12. Marine oxygen-isotope stages (MIS) and associated rainfall amounts are indicated for reference.

The modelled R_w (Eq. 11) ranges from 291 mm at 66.525 ky BP (MIS 4) to 1,063 mm at 82.325 ky BP (MIS 5a). There is no fixed relationship between R_w and stalagmite $\delta^{18}O_{iv}$ because the impact of R_w on $\delta^{18}O_{iv}$ varies as a function of mixing line slope.

However, R_w can be scaled to δ^{18}O in terms of differences, as follows:

$$\Delta R_w \propto \Delta^{18}O_w \quad (\text{where } \Delta R_w = R_w - 530 \text{ mm, and } \Delta^{18}O_w = \delta^{18}O_{iv} - \delta^{18}O_{si}) \tag{12}$$

Supplementary Figure 10 shows R_w scaled to the difference between the measured $\delta^{18}O_{iv}$ and the associated value of $\delta^{18}O_{si}$ on the summer in-mixing line ($\Delta^{18}O_w$). The results show that stalagmite $\delta^{18}O_{iv}$ is a factor of ~0.4 less sensitive, on average, to changes in R_w (with constant δ^{18}O) than to changes in R_s (with δ^{18}O that varies inversely with rainfall amount).

We assessed the sensitivity of the modelled rainfall to the use of –2‰ for the winter rainfall end-member $\delta^{18}O$ value in the mixing model. The winter value influences the slope of the summer in-mixing line (Eq. 2) and affects the resulting range of modelled summer rainfall. It is important to note, however, that the observed positive covariation between stalagmite K2 Mg/Ca and $\delta^{18}O$ across a broad range of climates could not occur if the $\delta^{18}O$ of winter rainfall varied significantly through time.

Currently, the trade wind temperature inversion layer caps atmospheric convection and limits cloud heights during winter in the tropics[22,23], resulting in the uniformly high $\delta^{18}O$ of winter rainfall in Indonesia[13], and elsewhere[24]. At Liang Luar, the amount-weighted average $\delta^{18}O$ for non-convective rainfall in 2006 was –1.9‰, similar to the longer-term dry-season average for Bali (–2.6‰ from 2003 to 2009)[4,13]. The $\delta^{18}O$ of dry-season rainfall in Bali also lies within a narrow range (–1.7 to –2.6‰) across the full range of mean monthly rainfall amounts (15–94 mm month^{-1}, Supplementary Fig. 7).

These observations support the use of a uniform $\delta^{18}O$ value of –2‰ for modelling the 40–110 mm month^{-1} range in winter rainfall represented in the K2 record. The relatively cool Indo-Pacific SSTs between 92 and 47 ky BP[12] would tend to stabilise the tradewind inversion[23], but we evaluated the effect of winter end-member $\delta^{18}O$ values ranging from –1‰ to –3‰ in the event that such modes were to occur at timescales exceeding the 50-year resolution of the K2 record. Results for the MIS 5b summer rainfall maximum and the MIS 3 minimum in the stalagmite K2 record are summarised below.

Modelled $\delta^{18}O_{si}$ (‰, VPDB)	R_s at R_w = –1‰ (mm)	R_s at R_w = –2‰ (mm)	R_s at R_w = –3‰ (mm)	Difference in R_s (–1) (mm relative to –2)	Difference in R_s (–3) (mm relative to -2)
MIS 5b (–7.0)	1056	1107	1197	–51	+90
Modern (–6.2)	870	870	870	0	0
MIS 3 (–3.5)	474	410	322	+64	–88

The overall pattern of rainfall change through time remains robust, with the lowest modelled summer rainfall during MIS 3. When the winter $\delta^{18}O$ was set to –1‰, the MIS 3 summer rainfall increased from 410 mm to 474 mm (+16%). In this case, the Eq. 2 slope-intercept relationship between $\delta^{18}O_{si}$ and the fraction of summer rainfall (F_s) becomes:

$$\delta^{18}O_{si} = -18.049F_s + 5.02 \tag{13}$$

And the resulting relationship between R_s and $\delta^{18}O_{si}$ (Eq. 6) is:

$$R_s = \frac{2660.6 - 530\delta^{18}O_{si}}{\delta^{18}O_{si} + 13.03} \tag{14}$$

Conversely, with winter at –3‰ the modelled MIS 3 summer rainfall decreased to 322 mm (–21‰). In this case, the Eq. 2 slope-intercept relationship for $\delta^{18}O_{si}$ and F_s becomes:

$$\delta^{18}O_{si} = -11.107F_s + 0.70 \tag{15}$$

And the resulting relationship between R_s and $\delta^{18}O_{si}$ (Eq. 6) is:

$$R_s = \frac{371.0 - 530\delta^{18}O_{si}}{\delta^{18}O_{si} + 10.41} \tag{16}$$

In both cases, the relatively wet summers during MIS 5b remain within 5–8% of their modelled values with winter set at –2‰.

Supplementary Note 3 Box 1: Ancillary information on the relationship between the $\delta^{18}O$ of summer rainfall and rainfall amount (as depicted in the inset plot for Supplementary Fig. 8)

The accuracy of the mixing model can be checked further by calculating the $\delta^{18}O$ for summer rainfall ($\delta^{18}O_s$) required to account for the range of $\delta^{18}O_{iv}$ in the K2 record for comparison with observational data for $\delta^{18}O_s$ in the region. Recall that the two end-member oxygen-isotope mass balance equation below describes the effect of variable contributions of summer and winter rainfall on stalagmite $\delta^{18}O_{iv}$ at any point within the mixing line array:

$$\delta^{18}O_{iv}\,(VPDB) = F_w * \delta^{18}O_w\,(VPDB_e) + F_s * \delta^{18}O_s\,(VPDB_e) \qquad \text{(a)}$$

Equation (a) can be rearranged to find $\delta^{18}O_s$ as a function of $\delta^{18}O_{iv}$. First, Eq. (a) is solved for F_s:

$$F_s = \frac{\delta^{18}O_{iv} - \delta^{18}O_w}{\delta^{18}O_s - \delta^{18}O_w} \qquad \text{(b)}$$

Substitution of Eq. 2 (in Note 3 above) into Eq. (b) yields the relationship among $\delta^{18}O_s$, $\delta^{18}O_{iv}$ and $\delta^{18}O_w$ at any point on the Eq. 2 summer in-mixing line in Supplementary Fig. 8:

$$\delta^{18}O_s = \frac{\delta^{18}O_{iv}\,(14.58 - \delta^{18}O_w) - 11.72\delta^{18}O_w}{2.86 - \delta^{18}O_{iv}} \qquad \text{(c)}$$

Substitution of –2‰ ($VPDB_e$) for $\delta^{18}O_w$ in Eq. (c) yields the relationship between $\delta^{18}O_s$ and $\delta^{18}O_{iv}$:

$$\delta^{18}O_s = \frac{23.44 + 16.58\delta^{18}O_{iv}}{2.86 - \delta^{18}O_{iv}} \qquad \text{(d)}$$

Note that for the model, $\delta^{18}O_s$ is expressed as a function of the ice-volume corrected $\delta^{18}O_{iv}$, and relative to the $\delta^{18}O$ of modern seawater. Thus, the true values of $\delta^{18}O_s$ would be slightly higher. Equation (d) shows that modelling of the –3.5‰ to –7‰ range in $\delta^{18}O_{iv}$ in the K2 record requires mixing lines with summer $\delta^{18}O_s$ values of –5.4‰ to –9.4‰ (Supplementary Fig. 8). The modelled range of 4‰ is well within the range of modern-day $\delta^{18}O_s$ at Liang Luar[4] and in southern Indonesia[13] (see Supplementary Fig. 7).

The mixing line array also can be checked by comparing the modelled $\delta^{18}O_s$ and modelled summer rainfall with observational data. Substitution of Eq. 2 into Eq. (d) yields $\delta^{18}O_s$ as a function of F_s below. Substitution of (R_s / $R_s + R_w$) for F_s (with winter rainfall (R_w) set to 530 mm), yields $\delta^{18}O_s$ in terms of summer rainfall (R_s):

$$\delta^{18}O_s = \frac{4.86}{F_s} - 16.58 = 4.86\left(\frac{530}{R_s}\right) - 11.72 \qquad \text{(e)}$$

Note that the modelled relationship between $\delta^{18}O_s$ and summer rainfall is not linear; $\delta^{18}O_s$ changes rapidly under drier climates and becomes less sensitive to changes in R_s under wetter conditions (see Supplementary Fig. 8 inset). The modern-day relationship between rainfall $\delta^{18}O$ and mean monthly rainfall at Makassar, south-western Sulawesi[13], near Flores, confirms this non-linear response. The seasonal range in rainfall at Makassar is exceptionally large (0–600 mm month^{-1}) and dominated strongly by changes in convective summer rainfall. The reduction in the rate of change in $\delta^{18}O_s$ as summer rainfall increases lends support to an association between the

"amount effect" and the intensity of convective monsoon rainfall[25,26]. This mechanism would rapidly decrease the $\delta^{18}O$ of rainfall at the onset of atmospheric convection (see effect in Fig. 4 of ref.[26]). On the other hand, the physical limit on convective cloud height would ultimately limit the lowering of $\delta^{18}O_s$ during exceptionally wet times. In the case of the K2 record, however, the relatively dry hydroclimate at Liang Luar from 91 to 47 ky BP means that $\delta^{18}O_{iv}$ is sensitive to the model-predicted rainfall amounts.

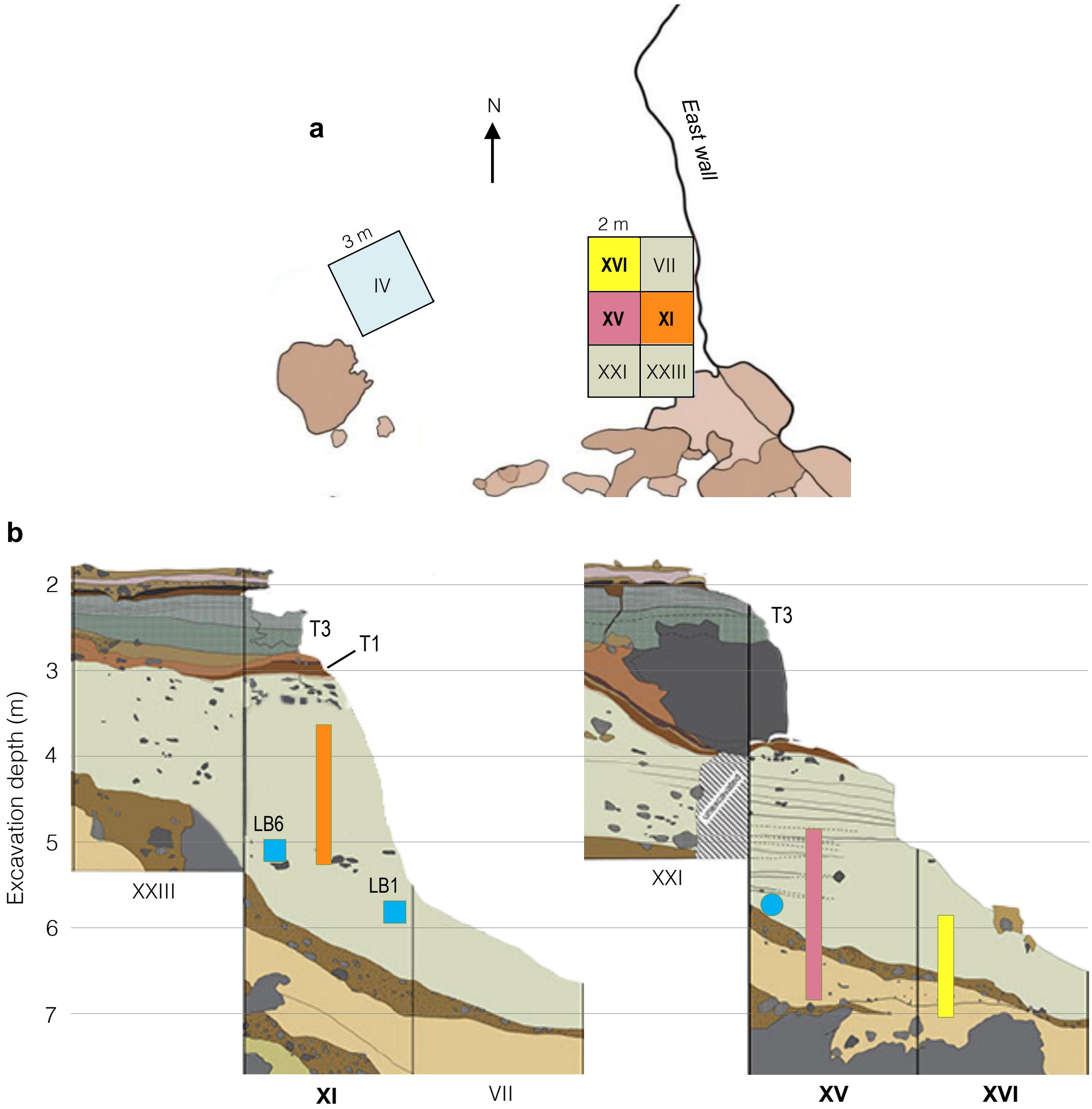

Supplementary Figure 11 | Stratigraphic context of *Stegodon florensis insularis* fossil tooth samples at Liang Bua (modified from Sutikna et al.[27]). **a** Plan view of the excavation sectors in the eastern half of Liang Bua noted in the text[27,28]. The *Stegodon* tooth enamel $\delta^{18}O$ age-depth series shown in Figure 7 is based on samples from Sectors XI, XV and XVI[29]. The fossil counts for *Stegodon* (and associated *Homo floresiensis*) presented in Figure 8 are based on skeletal remains from Sectors XI and IV[28,30,31]. **b** Stratigraphic depth-ranges of 27 *Stegodon* tooth samples analysed for $\delta^{18}O$ and $\delta^{13}C$ from Sectors XI (orange), XV (mauve) and XVI (yellow)[29] (see Supplementary Table 2). The parallel cross-sections are 4 m apart and face westward toward the centre of the cave. The *Stegodon* and *H. floresiensis*-bearing colluvial deposits (pale green) overlie a gravel-rich layer (brown). All tooth samples were collected below the overlying volcanic tephra T1 (brown). The four deepest samples in Sectors XV and XVI were within the gravel-rich layer and an underlying reddish-brown clayey deposit. Blue squares indicate the locations of U-Th dated *H. floresiensis* ulnae in Sector XI: LB1 (79.1 ± 8.9 ka at 5.8 m) and LB6 (59.8 ± 3.8 ka at 5.1 m); dates (±2 SE) are weighted averages based on repeat measurements[27]. A thermoluminescence age of 89 ± 7 ka (2σ) was obtained for sediment sample LB08-15-3 (5.73 m, blue circle) near the base of the *H. floresiensis*-bearing deposits in Sector XV[27]. The fossil-bearing deposits slope gently northward, thus the tooth $\delta^{18}O$ data for Sector XVI (n = 4), located downslope, were adjusted upward by –0.2 m depth (equivalent to –1.8 ky) for temporal alignment with samples in Sectors XI and XV for the age-depth comparison shown in Figure 7. The horizontal positions of the coloured bars are schematic.

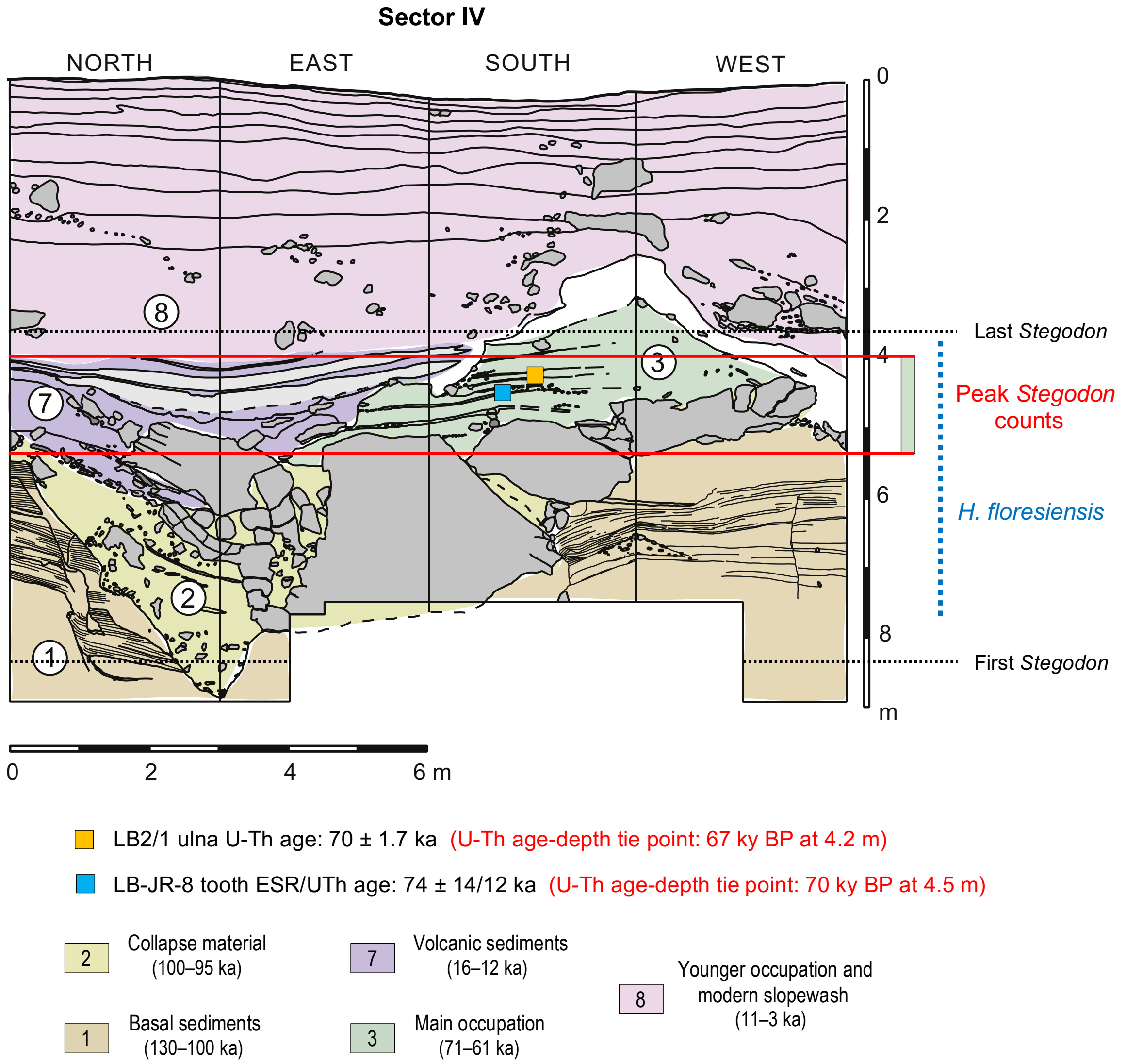

Supplementary Figure 12 | Stratigraphic context and age of the fossil-bearing deposits in excavation Sector IV (modified from Westaway et al.[32]). Sector IV yielded 313 skeletal elements attributable to *Stegodon florensis insularis* between 8.35 m and 3.65 m and associated *Homo floresiensis* remains between 7.65 m and 3.75 m (refs.[28,31,33]). The gently sloping, fossil-rich colluvial deposits exposed in the southern half of Sector IV (pale green) were previously assigned to 74–61 ka (Unit 3 in ref.[32]), based on chronological data summarised by Roberts et al.[34]. A new U-Th date on an *H. floresiensis* ulna (LB2/1, 70 ± 1.7 ka, orange square) [27] is consistent with a previously reported coupled ESR/UTh date for a nearby juvenile *Stegodon* tooth (LB-JR-8, 74 ± 14/12 ka, blue square)[28]. The good agreement of the new U-Th tie point ages (shown in red text) provides further evidence for stratigraphic continuity of the fossil-bearing deposits between sectors IV and XI (located ~11 m apart). The northern half of Sector IV contains collapse material and more recent infill, but this does not significantly affect the proportional representation of *Stegodon* and *H. floresiensis* fossils. No remains of either species were detected in sieved sediments above 3.65 m[31] (overlying the fossil-bearing deposits), or in the younger volcanic-rich Unit 7 exposed in the eastern and northern excavation baulks. Given the stratigraphic and chronological similarities between sectors IV and XI, the best-fit chronological alignment of *Stegodon* and *H. floresiensis* fossil counts is presented in Figure 8, with a minor depth correction for Sector IV (–0.2 m depth, equivalent to –1.8 ky).

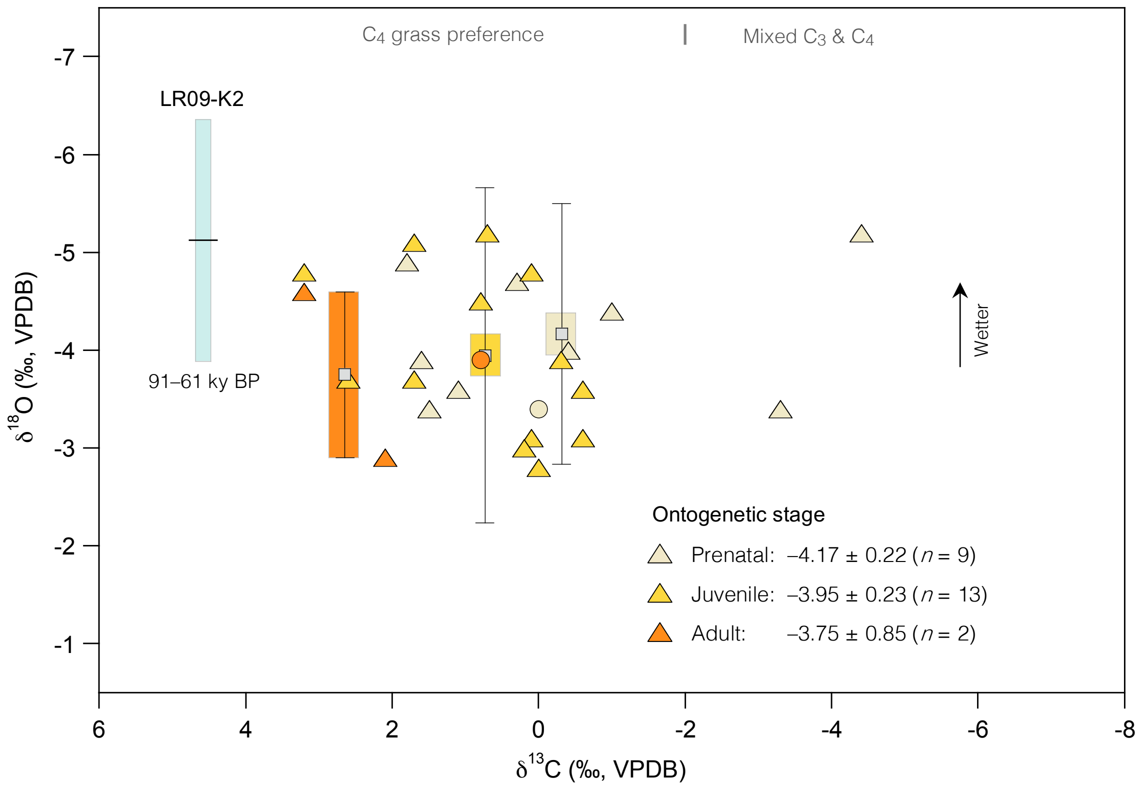

Supplementary Figure 13 | $\delta^{18}O$ and $\delta^{13}C$ of *Stegodon florensis insularis* fossil tooth enamel at different ontogenetic stages. $\delta^{18}O$ and $\delta^{13}C$ data are shown for *S. florensis insularis* tooth samples from Sectors XI, XV and XVI at Liang Bua formed at prenatal, juvenile, and adult ontogenetic stages[29] (see Supplementary Table 2). Colour-coded boxes represent the standard error of the mean (±SE) for each $\delta^{18}O$ dataset; vertical black bars indicate two standard deviations (±2σ). The summary statistics show no significant difference in the mean $\delta^{18}O$ values (±SE) for the prenatal and juvenile groups. The consistent mean values support comparison of the subadult $\delta^{18}O$ data for Liang Bua with the stalagmite K2 $\delta^{18}O$ time series for Liang Luar (excluding one outlier identified in Figure 7, shown as a tan circle). The three adult molars are too few for statistical analysis, but the $\delta^{18}O$ values for two specimens (triangles) are well aligned with the K2 $\delta^{18}O$ record. The blue bar shows the similar range of the K2 $\delta^{18}O$ data (mean ±2σ, not corrected for ice-volume effect) and tooth $\delta^{18}O$ data across the age-depth calibration interval in Figure 7 (91–61 ky BP). The tooth $\delta^{13}C$ values (with the exception of two prenatal samples) indicate that *S. florensis insularis* was primarily a C_4 grazer[29].

Supplementary Table 1: U-Th isotope data for stalagmite LR09-K2. ^{230}Th ages were calculated using the half-lives for ^{234}U (245,620 ± 70 y) and ^{230}Th (75,584 ± 30 y) determined by Cheng et al.[35]. Corrected ^{230}Th ages were calculated using the bulk Earth initial ^{230}Th/^{232}Th activity value of 0.82 ± 0.41. "Age (y BP)" gives ages in years before the present, with present defined as the year 1950 CE. The three dates in italics were not used in the final age-depth model. All uncertainties are quoted at ±2σ.

Sample ID	Lab / year	Depth (mm from top)	^{238}U (ppb)	^{232}Th (ppt)	^{230}Th / ^{232}Th (activity)	^{230}Th / ^{238}U (activity)	δ^{234}U (measured)	^{230}Th age (y) (uncorrected)	^{230}Th age (y) (corrected)	$\delta^{234}U_{initial}$ (corrected)	^{230}Th age (y BP) (corrected)
LR09-K2-M1	UMinn / 2015	35	161.3 ±0.2	198 ±4	948 ±19	0.3790 ±0.0006	57.3 ±1.4	48187 ±146	48152 ±147	66 ±2	**48087 ±147**
LR09-K2-M2	UMinn / 2015	139.5	231.9 ±0.3	164 ±3	1756 ±36	0.4043 ±0.0007	56.7 ±1.6	52328 ±175	52311 ±177	66 ±2	**52246 ±177**
LR09-K2-M3	UMinn / 2015	233	311.4 ±0.4	239 ±5	1661 ±34	0.4147 ±0.0007	51.9 ±1.4	54402 ±174	54381 ±175	61 ±2	**54316 ±175**
LR09-K2-M4	UMinn / 2015	302.5	199.9 ±0.2	85 ±2	2996 ±67	0.4156 ±0.0007	53.0 ±1.3	54477 ±167	54465 ±170	62 ±1	**54400 ±170**
LR09-K2-U02	UMinn / 2013	315.5	176.7 ±0.2	264 ±5	859 ±18	0.4172 ±0.0009	52.9 ±1.6	54755 ±209	54716 ±211	62 ±2	**54653 ±211**
LR09-K2-M5	UMinn / 2015	417	426.0 ±0.6	46 ±1	12136 ±286	0.4302 ±0.0007	49.0 ±1.3	57281 ±178	57277 ±179	58 ±2	**57212 ±179**
LR09-K2-M6	UMinn / 2015	526.5	250.8 ±0.3	129 ±3	2615 ±55	0.4381 ±0.0008	42.8 ±1.7	59165 ±215	59150 ±217	51 ±2	**59085 ±217**
LR09-K2-04	UMelb / 2010	539	440 ±33		1046	0.4417 ±0.0023	48.9 ±2.2	59313 ±451	59274 ±455	58 ±3	**59214 ±455**
LR09-K2-U04	UMinn / 2012	642.5	493.0 ±0.9	146 ±3	4602 ±96	0.4437 ±0.0009	48.0 ±2.0	59742 ±245	59732 ±246	57 ±2	**59670 ±246**
LR09-K2-U06	UMinn / 2012	707.5	265.2 ±0.3	19 ±1	19073 ±1231	0.4515 ±0.0008	49.6 ±1.5	61010 ±211	61005 ±211	59 ±2	**60943 ±211**
LR09-K2-U10	UMinn / 2012	805	161.7 ±0.2	597 ±12	387 ±8	0.4640 ±0.0010	49.0 ±1.9	63336 ±269	63235 ±277	59 ±2	**63173 ±277**
LR09-K2-U17	UMinn / 2012	838.5	52.1 ±0.1	116 ±3	656 ±15	0.4757 ±0.0022	46.2 ±2.5	65771 ±482	65709 ±488	56 ±3	**65647 ±488**
LR09-K2-U19	UMinn / 2013	847	56.2 ±0.1	94 ±2	879 ±21	0.4794 ±0.0016	47.1 ±1.5	66389 ±349	66343 ±355	57 ±2	**66280 ±355**
LR09-K2-U21	UMinn / 2012	852	112.2 ±0.1	10 ±1	17498 ±1959	0.4910 ±0.0012	46.8 ±1.7	68636 ±305	68637 ±305	57 ±2	**68575 ±305**
LR09-K2-M7	UMinn / 2015	853.5	124.2 ±0.1	6 ±1	29195 ±3248	0.4913 ±0.0009	46.0 ±1.7	68775 ±263	68775 ±263	56 ±2	**68710 ±263**
LR09-K2-05	*UMelb / 2010*	*858*	*164 ±12*		*2783*	*0.4922 ±0.0028*	*50.4 ±2.2*	*68513 ±589*	*68506 ±592*	*61 ±3*	***68446 ±592***
LR09-K2-U25	UMinn / 2012	872.5	137.9 ±0.2	35 ±1	6063 ±213	0.4992 ±0.0010	45.6 ±1.9	70362 ±295	70354 ±297	56 ±2	**70292 ±297**
LR09-K2-M8	UMinn / 2015	887.5	184.6 ±0.2	68 ±1	4189 ±92	0.4998 ±0.0008	42.3 ±1.6	70819 ±252	70809 ±253	52 ±2	**70744 ±253**
LR09-K2-U27	UMinn / 2012	900	124.7 ±0.1	47 ±1	4141 ±126	0.5041 ±0.0011	49.2 ±1.7	70956 ±298	70949 ±300	60 ±2	**70887 ±300**
LR09-K2-M9	*UMinn / 2015*	*917.5*	*136.9 ±0.2*	*33 ±1*	*6349 ±191*	*0.4991 ±0.0009*	*42.3 ±1.8*	*70669 ±263*	*70662 ±263*	*52 ±2*	***70597 ±263***
LR09-K2-M10	UMinn / 2015	938.5	216.6 ±0.3	9 ±1	36166 ±2184	0.5007 ±0.0010	41.8 ±1.5	71052 ±276	71048 ±276	51 ±2	**70983 ±276**
LR09-K2-06	UMelb / 2010	940	230 ±17		10030	0.5039 ±0.0020	46.4 ±2.1	71206 ±465	71205 ±465	57 ±3	**71145 ±465**
LR09-K2-M11	UMinn / 2015	993.5	131.5 ±0.2	6 ±1	33479 ±2711	0.5074 ±0.0009	44.7 ±1.5	72083 ±265	72083 ±265	55 ±2	**72018 ±265**
LR09-K2-M12	UMinn / 2015	1048	143.4 ±0.2	27 ±1	8394 ±249	0.5117 ±0.0009	44.9 ±1.7	72929 ±277	72924 ±278	55 ±2	**72859 ±278**
LR09-K2-M13	UMinn / 2015	1073.5	142.9 ±0.1	9 ±1	26866 ±2360	0.5290 ±0.0009	39.2 ±1.6	77138 ±290	77136 ±291	49 ±2	**77071 ±291**
LR09-K2-M14	UMinn / 2015	1104	102.1 ±0.1	33 ±1	5143 ±143	0.5425 ±0.0011	38.7 ±1.7	80087 ±342	80077 ±343	48 ±2	**80012 ±343**
LR09-K2-M15	UMinn / 2015	1133.5	97.6 ±0.1	5 ±1	36192 ±4099	0.5479 ±0.0009	40.1 ±1.4	81084 ±289	81084 ±290	50 ±2	**81019 ±290**
LR09-K2-07	UMelb / 2010	1150	190 ±14		2833	0.5641 ±0.0033	42.8 ±2.5	84315 ±823	84300 ±830	54 ±3	**84240 ±830**
LR09-K2-M16	UMinn / 2015	1152	182.2 ±0.2	2 ±1	132884 ±34774	0.5635 ±0.0009	42.0 ±1.2	84287 ±284	84287 ±284	53 ±2	**84222 ±284**

Supplementary Table 1 (continued)

Sample ID	Lab / year	Depth (mm from top)	^{238}U (ppb)	^{232}Th (ppt)	^{230}Th / ^{232}Th (activity)	^{230}Th / ^{238}U (activity)	$\delta^{234}U$ (measured)	^{230}Th age (y) (uncorrected)	^{230}Th age (y) (corrected)	$\delta^{234}U_{initial}$ (corrected)	^{230}Th age (y BP) (corrected)
LR09-K2-M17	UMinn / 2015	1208	156.3 ±0.1	2 ±1	156194 ±60339	0.5731 ±0.0009	41.7 ±1.4	86507 ±309	86507 ±309	53 ±2	**86442 ±309**
LR09-K2-08	UMelb / 2010	1261	128 ±10		1777	0.5813 ±0.0032	39.0 ±2.5	88785 ±849	88760 ±854	50 ±3	**88700 ±854**
LR09-K2-M18	UMinn / 2015	1278.5	220.5 ±0.2	92 ±2	4325 ±91	0.5860 ±0.0008	39.4 ±1.4	89835 ±310	89824 ±312	51 ±2	**89759 ±312**
LR09-K2-M19	*UMinn / 2015*	*1308*	*182.8 ±0.2*	*219 ±4*	*1516 ±31*	*0.5913 ±0.0010*	*40.6 ±1.7*	*90906 ±344*	*90873 ±345*	*53 ±2*	***90808 ±345***
LR09-K2-09	UMelb / 2010	1408	251 ±19		428	0.5929 ±0.0020	42.1 ±2.1	91068 ±592	90952 ±599	54 ±3	**90892 ±599**
LR09-K2-M20	UMinn / 2015	1526	252.1 ±0.3	111 ±2	4175 ±88	0.5949 ±0.0010	44.5 ±1.5	91185 ±349	91170 ±353	58 ±2	**91105 ±353**

Supplementary Table 2: δ^{18}O and δ^{13}C results and U-Th tie-point ages for *Stegodon florensis insularis* tooth enamel (based on stable-isotope data in Appendix II of Puspaningrum[29]). Tie-point ages were calculated using the oxygen-isotope age-depth relationship in Figure 7: age (ky BP) = 9.11*depth (m) + 28.2. Three δ^{18}O values (underlined) were identified as outliers from the relationship. The excavation depths for Sector XVI (italicised) are adjusted by –0.2 m (1.8 ky to younger) for temporal alignment with Sector XV. See Puspaningrum[29] for details on the dental formula used to classify each tooth.

Tooth sample ID	Excavation depth (m)	U-Th tie-point age (ky BP)	δ^{18}O (‰, VPDB)	δ^{13}C (‰, VPDB)	Dental morphology and ontogenetic stage
Sector XI					
LB04-SXI-Sp37-1	3.65–3.75	61.9	-4.4	-1.0	prenatal: milk tusk frag.
LB04-SXI-Sp38b-2	3.75–3.85	62.8	-3.4	-3.3	prenatal: dex dP_3 frag.
LB04-SXI-Sp40-3	3.95–4.05	64.6	-4.9	1.8	prenatal: milk tusk frag.
LB04-SXI-Sp41-4	4.05–4.15	65.6	-5.1	1.7	juvenile: dP4-M1 frag.
LB04-SXI-Sp42-6a	4.15–4.25	66.5	-4.6	3.2	adult: M2 frag.
LB04-SXI-Sp42-6b	4.15–4.25	66.5	-3.4	0.0	prenatal: dP_3 frag.
LB04-SXI-Sp44-7	4.35–4.45	68.3	-4.7	0.3	prenatal: dP_3
LB04-SXI-Sp45-449B	4.45–4.55	69.2	-3.1	0.1	juvenile: post. dex dP^4
LB04-SXI-Sp45-453	4.45–4.55	69.2	-3.9	-0.3	juvenile: dP^4 frag.
LB04-SXI-Sp46-456	4.55–4.65	70.1	-2.9	2.1	adult: dex M_2
LB04-SXI-Sp47-521F	4.65–4.75	71.0	-3.1	-0.6	juvenile: M^1 frag.
LB04-SXI-Sp47-521F	4.65–4.75	71.0	-2.8	0.0	juvenile: dP^4 frag.
LB04-SXI-Sp48-608	4.75–4.85	71.9	-4.8	0.1	juvenile: M_1 sin
LB04-SXI-Sp49	4.85–4.95	72.8	-3.7	1.7	juvenile: dP^4 frag.
LB04-SXI-Sp49-669F	4.85–4.95	72.8	-3.0	0.2	juvenile: ant. sin. M^1 frag.
LB04-SXI-Sp49-12-669g	4.85–4.95	72.8	-4.8	3.2	juvenile: dex M^1 frag.
LB04-SXI-Sp52-14-803a	5.15–5.25	75.6	-5.5	1.6	unclassified molar frag.
Sector XV					
LB08-SXV-Sp49	4.85–4.95	72.8	-3.7	2.6	juvenile: dP4-M1 ridge frag.
LB08-SXV-Sp55-2042A	5.45–5.55	78.3	-3.6	1.1	prenatal: dP^3 sin
LB08-SXV-Sp57-2056B	5.65–5.75	80.1	-4.0	-0.4	prenatal: sin dP_3
LB09-SXV-Sp62	6.15–6.25	84.7	-3.4	1.5	prenatal: dP_3 ridge frag.
LB08-SXV-Sp65	6.45–6.55	87.4	-4.5	0.8	juvenile: dP^4 ridge frag.
LB09-SXV-Sp68	6.75–6.85	90.1	-5.2	-4.4	prenatal: dP_3 frag.
Sector XVI					
LB08-SXVI-Sp59-16	*5.65–5.75*	*80.1*	-3.9	1.6	prenatal: dP_3 frag.
LB08-SXVI-Sp64-17-3495	*6.15–6.25*	*84.7*	-3.6	-0.6	juvenile: M1
LB08-SXVI-Sp70-3631	*6.75–6.85*	*90.1*	-3.9	0.8	adult: maxilla with M^3 frag
LB08-SXVI-Sp70-18-3613	*6.75–6.85*	*90.1*	-5.2	0.7	juvenile: dP4-M1 frag.
Sectors XIX and XII					
LB09-SXIX-Sp33	3.25–3.35	na	-3.3	0.2	prenatal: sin dP_3
LB07-SXII-Sp41	4.05–4.15	na	-2.9	0.1	juvenile: dex M^1

Supplementary Table 3: Chronology of *Stegodon florensis insularis* and *Homo floresiensis* faunal counts (based on faunal data in Appendix A of van den Bergh *et al.*[31]). Tie-point ages were calculated using the oxygen-isotope age-depth relationship in Figure 7: age (ky BP) = 9.11*depth (m) + 28.2. The excavation depths for Sector IV are adjusted by –0.2 m (1.8 ky to younger) for temporal alignment with Sector XI. Significant *H. floresiensis* specimens are noted by LB identification numbers reported in Morwood *et al.*[30] for Sector XI and Morwood and Jungers[33] for Sector IV.

Excavation depth (m)	U-Th tie-point age (ky BP)	Sector XI (number of specimens)		Sector IV (number of specimens)	
		S. florensis insularis	*H. floresiensis*	*S. florensis insularis*	*H. floresiensis*
3.05–3.15	56.4	*Volcanic tephra layer T1*		*Erosion and formation of flowstone*	
3.15–3.25	57.4	3	0	0	0
3.25–3.35	58.3	0	0	0	0
3.35–3.45	59.2	0	0	0	0
3.45–3.55	60.1	2	0	2	0
3.55–3.65	61.0	2	1	1	1
3.65–3.75	61.9	1	0	6	0
3.75–3.85	62.8	6	0	7	0
3.85–3.95	63.7	14	0	10	0
3.95–4.05	64.6	25	0	14	3 (LB2)
4.05–4.15	65.6	23	0	23	2 (LB2)
4.15–4.25	66.5	49	1 (LB4)	16	0
4.25–4.35	67.4	17	1 (LB4)	34	4
4.35–4.45	68.3	28	1	14	0
4.45–4.55	69.2	49	0	18	1 (LB10)
4.55–4.65	70.1	52	2 (LB5)	16	0
4.65–4.75	71.0	51	0	14	0
4.75–4.85	71.9	28	0	9	1
4.85–4.95	72.8	30	0	17	0
4.95–5.05	73.8	36	0	13	4 (LB11)
5.05–5.15	74.7	35	7 (LB6)	20	1 (LB11)
5.15–5.25	75.6	19	6 (LB6)	22	0
5.25–5.35	76.5	5	1 (LB6)	9	0
5.35–5.45	77.4	1	0	1	5
5.45–5.55	78.3	2	0	5	0
5.55–5.65	79.2	0	1 (LB7)	2	1 (LB3)
5.65–5.75	80.1	0	3	1	0
5.75–5.85	81.0	0	5 (LB1/LB8)	0	0
5.85–5.95	82.0	1	0	1	0
5.95–6.05	82.9	1	0	1	1
6.05–6.15	83.8	0	0	1	0
6.15–6.25	84.7	1	0	1	1
6.25–6.35	85.6	1	0	0	0
6.35–6.45	86.5	1	0	0	0
6.45–6.55	87.4	1	1 (LB9)	0	0
6.55–6.65	88.3	0	0	0	0
6.65–6.75	89.2	1	0	0	0
6.75–6.85	90.2	0	0	1	0
6.85–6.95	91.1	1	0	4	0
6.95–7.05	92.0	0	0	2	0

Excavations continue downward to 8.75 m (Sector XI) and 8.45 m (Sector IV)

Supplementary References

1. Bronk Ramsey, C. Deposition models for chronological records. *Quat. Sci. Rev.* **27**, 42–60 (2008).
2. Bronk Ramsey, C. & Lee, S. Recent and planned developments of the program OxCal. *Radiocarbon* **55**, 720–730 (2013).
3. Scroxton, N. *et al.* Antiphase response of the Indonesian-Australian monsoon to millennial-scale events of the last glacial period. *Sci. Rpt.* 1**2**, 21512, doi.org/10.1038/s41598-022-25810-1 (2022).
4. Griffiths, M. L. *et al.* Increasing Australian-Indonesian monsoon rainfall linked to early Holocene sea-level rise. *Nat. Geosci.* **2**, 636–639 (2009).
5. Lewis, S. C. *et al.* High-resolution stalagmite reconstructions of Australian-Indonesian monsoon rainfall variability during Heinrich Stadial 3 and Greenland Interstadial 4. *Earth Planet. Sci. Lett.* **303**, 133–142 (2011).
6. Ayliffe, L. K. *et al.* Rapid interhemispheric climate links via the Australasian monsoon during the last deglaciation. *Nat. Commun.* **4**, 2908, doi:10.1038/ncomms3908 (2013).
7. Griffiths, M. L. *et al.* Australasian monsoon response to Dansgaard-Oeschger event 21 and teleconnections to higher latitudes. *Earth Planet. Sci. Lett.* **369-370**, 294–304 (2013).
8. Sinclair, D. *et al.* Magnesium and strontium systematics in tropical speleothems from the Western Pacific. *Chem. Geol.* **294-295**, 1–17 (2012).
9. Huang, Y. & Fairchild, I. J. Partitioning of Sr^{2+} and Mg^{2+} into calcite under karst-analogue experimental conditions. *Geochim. Cosmochim. Acta* **65**, 47–62 (2001).
10. Wassenburg, J. A. *et al.* Calcite Mg and Sr partition coefficients in cave environments: Implications for interpreting prior calcite precipitation in speleothems. *Geochim. Cosmochim. Acta* **269**, 581–596 (2020).
11. Kulp, J. L., Turekian, K. & Boyd, D. W. Strontium content of limestones and fossils. *Bull. Geol. Soc. Amer.* **63**, 701–716 (1952).
12. Lea, D. W., Pak, D. K. & Spero, H. J. Climate impact of Late Quaternary equatorial Pacific sea surface temperature variations. *Science* **289**, 1719–1724 (2000).
13. Kurita, N., Ichiyanagi, K., Matsumoto, J., Yamanaka, M. D. & Ohata, T. The relationship between the isotopic content of precipitation and the precipitation amount in tropical regions. *J. Geochem. Explor*. **102**, 113–122 (2009).
14. Acker, J. G. & Leptoukh, G. Online analysis enhances use of NASA earth science data. *Eos* **88**, doi:10.1029/2007EO020003 (2007).
15. Huffman, G. *et al.* The TRMM multisatellite precipitation analysis (TMPA): Quasi-global, multiyear, combined-sensor precipitation estimates at fine scales. *J. Hydrometeorol.* **8**, 38–55 (2007).
16. Lawrimore, J. H. *et al.* Global Historical Climatology Network - Monthly (GHCN-M) Version 4. NOAA National Centers for Environmental Information. https://doi.org/10.7289/V5X34VDR (2011).
17. Putman, A. L., Fiorella, R. P., Bowen, G. J. & Cai, Z. A global perspective on local meteoric water lines: meta-analytic insight into fundamental controls and practical constraints. *J. Water Resour. Res.* **55**, 6896–6910 (2019).
18. Griffiths, M. L. *et al.* Younger Dryas–Holocene temperature and rainfall history of southern Indonesia from $\delta^{18}O$ in speleothem calcite and fluid inclusions. *Earth Planet. Sci. Lett.* **295**, 30–36 (2010).
19. Coplen, T. B., Kendall, C. & Hopple, J. Comparison of stable isotope reference samples. *Nature* **302**, 236–238 (1983).
20. Krause, C. E. *et al.* Spatio-temporal evolution of the Australasian monsoon hydroclimate over the last 40,000 years. *Earth Planet. Sci. Lett.* **513**, 103–112 (2019).
21. Kimbrough, A. K. *et al.* Multi-proxy validation of glacial-interglacial rainfall variations in southwest Sulawesi. *Commun. Earth Environ*. **4**, 210, doi.org/10.1038/s43247-023-00873-8 (2023).

22. Permana, D. S., Thompson, L. G. & Setyadi, G. Tropical West Pacific moisture dynamics and climate controls on rainfall isotopic ratios in southern Papua, Indonesia. *J. Geophys. Res. Atmos.* **121**, 2222–2245 (2016).

23. Schubert, W. H., Ciesielski, P. E., Lu, C. & Johnson, R. H. Dynamical adjustment of the trade wind inversion layer. *J. Atmos. Sci.* **52**, 2941–2952 (1995).

24. Scholl, M. A, Giambelluca, T. W., Gingerich, S. B., Nullet, M. A. & Loope, L. L. Cloud water in windward and leeward mountain forests: the stable isotope signature of orographic cloud water. *Water Resour. Res.* **43**, W12411, doi:10.1029/2007WR006011 (2007).

25. Kurita, N. Water isotope variability in response to mesoscale convective system over the tropical ocean. *J. Geophys. Res. Atmos.* **118**, 10376–10390 (2013).

26. Yu, W. *et al.* Water isotope ratios reflect convection intensity rather than rain type proportions in the pantropics. *Sci. Adv.* **10**, eado3258 (2024).

27. Sutikna, T. *et al.* Revised stratigraphy and chronology for *Homo floresiensis* at Liang Bua in Indonesia. *Nature* **532**, 366–369 (2016).

28. Morwood, M. J. *et al.* Archaeology and age of a new hominin from Flores in eastern Indonesia. *Nature* **431**, 1087–1091 (2004).

29. Puspaningrum, M. R. *Proboscidea as Palaeoenvironmental Indicators in Southeast Asia*. PhD thesis, School of Earth and Environmental Sciences, University of Wollongong, 2016. https://ro.uow.edu.au/theses/4944.

30. Morwood, M. J. *et al.* Further evidence for small-bodied hominins from the Late Pleistocene of Flores, Indonesia. *Nature* **437**, 1012–1017 (2005).

31. van den Bergh, G. D. *et al.* The Liang Bua faunal remains: a 95 k.yr. sequence from Flores, East Indonesia. *J. Hum. Evol.* **57**, 527–537 (2009).

32. Westaway, K. E. *et al. Homo floresiensis* and the late Pleistocene environments of eastern Indonesia: defining the nature of the relationship. *Quat. Sci. Rev.* **28**, 2897–2912 (2009).

33. Morwood, M. J. & Jungers, W. L. Conclusions: implications of the Liang Bua excavations for hominin evolution and biogeography. *J. Hum. Evol.* **57**, 640–648 (2009).

34. Roberts, R. G. *et al.* Geochronology of cave deposits at Liang Bua and of adjacent river terraces in the Wae Racang valley, western Flores, Indonesia: a synthesis of age estimates for the type locality of *Homo floresiensis*. *J. Hum. Evol.* **57**, 484–502 (2009).

35. Cheng, H. *et al.* Improvements in ^{230}Th dating, ^{230}Th and ^{234}U half-life values, and U-Th isotopic measurements by multi-collector inductively coupled plasma mass spectrometry. *Earth Planet. Sci. Lett.* **371**, 82–91 (2013).